Cell Reports

Stem cell-derived vessels-on-chip for cardiovascular disease modeling

Graphical abstract

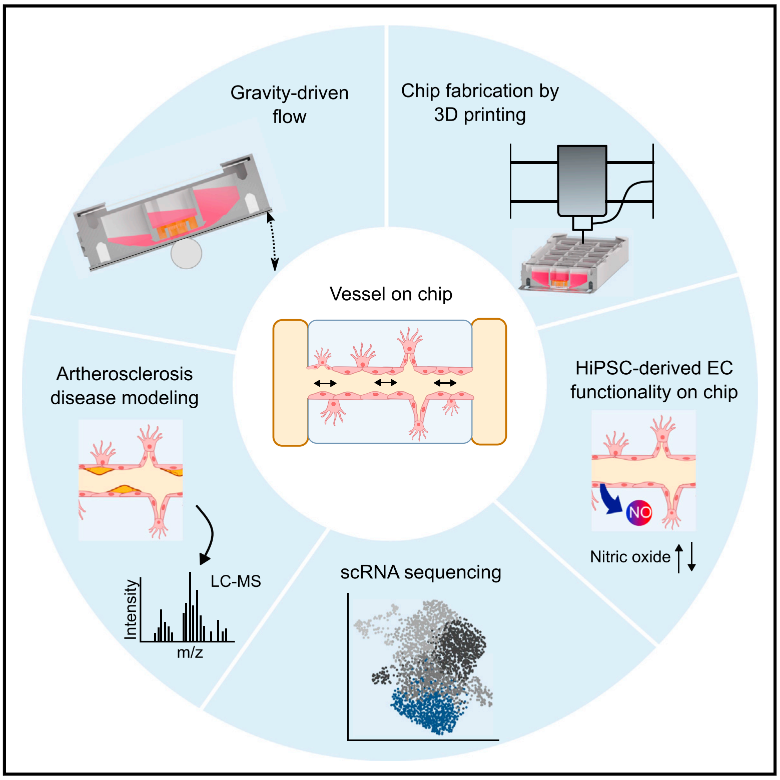

Highlights

- Engineering of a scalable open microfluidic chip platform for endothelial vessels
- Flow induction improves barrier function and increases NO synthesis of ECs
- Single-cell RNA sequencing reveals maturation of stem cell-derived ECs
- Modeling of atherosclerosis onset by oxidative stress on-chip

Authors

Maren Marder, Caroline Remmert, Julius A. Perschel, ..., Bilal Sheikh, Michel Moussus, Matthias Meier

Correspondence

matthias.meier@helmholtz-munich.de

In brief

Marder et al. engineered an open microfluidic vessel-on-chip platform for multiomics cell analysis. We demonstrated that flow induction on the chip led to the formation and maturation of functional vessels from stem cell-derived endothelial cells. Upon applying oxidative stress to the vessels-on-chip, the early onset of cardiovascular disease was investigated.

Marder et al., 2024, Cell Reports *43*, 114008
April 23, 2024
https://doi.org/10.1016/j.celrep.2024.114008

Cell Reports

CellPress
OPEN ACCESS

Article

Stem cell-derived vessels-on-chip for cardiovascular disease modeling

Maren Marder,[1,7] Caroline Remmert,[1,7] Julius A. Perschel,[1] Munkhtur Otgonbayar,[1] Christine von Toerne,[2] Stefanie Hauck,[2] Judith Bushe,[3] Annette Feuchtinger,[3] Bilal Sheikh,[4,5] Michel Moussus,[1] and Matthias Meier[1,6,8,*]
[1]Helmholtz Pioneer Campus, Helmholtz Zentrum München, Munich, Germany
[2]Metabolomics and Proteomics Core, Helmholtz Zentrum München, Munich, Germany
[3]Core Facility Pathology & Tissue Analytics, Helmholtz Munich, 85764 Neuherberg, Germany
[4]Helmholtz Institute for Metabolic, Obesity and Vascular Research (HI-MAG) of the Helmholtz Center Munich, Leipzig, Germany
[5]Medical Faculty, University of Leipzig, Leipzig, Germany
[6]Centre for Biotechnology and Biomedicine, University of Leipzig, Leipzig, Germany
[7]These authors contributed equally
[8]Lead contact
*Correspondence: matthias.meier@helmholtz-munich.de
https://doi.org/10.1016/j.celrep.2024.114008

SUMMARY

The metabolic syndrome is accompanied by vascular complications. Human *in vitro* disease models are hence required to better understand vascular dysfunctions and guide clinical therapies. Here, we engineered an open microfluidic vessel-on-chip platform that integrates human pluripotent stem cell-derived endothelial cells (SC-ECs). The open microfluidic design enables seamless integration with state-of-the-art analytical technologies, including single-cell RNA sequencing, proteomics by mass spectrometry, and high-resolution imaging. Beyond previous systems, we report SC-EC maturation by means of barrier formation, arterial toning, and high nitric oxide synthesis levels under gravity-driven flow. Functionally, we corroborate the hallmarks of early-onset atherosclerosis with low sample volumes and cell numbers under flow conditions by determining proteome and secretome changes in SC-ECs stimulated with oxidized low-density lipoprotein and free fatty acids. More broadly, our organ-on-chip platform enables the modeling of patient-specific human endothelial tissue and has the potential to become a general tool for animal-free vascular research.

INTRODUCTION

The human vascular system is a highly organized and dynamic cellular network responsible for maintaining homeostasis in all organs. Endothelial cells (ECs) are the central cell type of the vascular system, which forms the inner wall layer of the blood and lymphatic vessels and thus regulates blood flow, immune cell trafficking, and oxygen and nutrient delivery.[1] To comply with the multiple functions in the different organs, ECs are highly plastic and heterogeneous. Single-cell transcriptomics has confirmed the trans- and intra-tissue EC heterogeneity,[2] but how the heterogeneity evolves and which microenvironmental factors shape EC states remain unclear. Understanding EC development, adaptation, and response to microenvironmental cues is of central importance for revealing dysfunctions in the vascular network (for example, in chronic metabolic syndromes such as obesity, diabetes, and aging.)[3]

Reliable human *in vitro* models for endothelial tissues and the vasculature are in urgent demand, given the complexity of the human vascular system and proven metabolic distance of rodent *in vivo* models to human biology.[4] Cardiovascular damage is an intrinsically slow process, particularly when caused by metabolic syndromes.[5] Engineered, stable cell types that carry genetic predispositions to vascular diseases are hence best suited to recapitulate human vessels *in vitro*. Human inducible pluripotent stem cells (hiPSCs) present an almost unlimited EC source with highly reproducible phenotypes.[6] Various differentiation protocols have been developed to engineer stem cell-derived ECs (SC-ECs).[7] Upon culturing SC-ECs in a hydrogel environment, tubular microvessel structures were formed, and single-cell transcriptomic analysis resolved transcriptional changes during their formation, including sprouting, coalescence, and tubulogenic cell states.[8] However, SC-ECs within microvessels exhibited only immature and nonspecialized characters.[9–11] While mechanical properties of SC-ECs within organoid and hydrogel cultures can be modulated, the shear flow cannot due to missing accessibility of the microvessel luminal site. However, shear flow regulates various EC functions, such as proliferation and differentiation, through transcriptomic changes.[12,13]

Attempts to expose ECs to flow shear forces have been limited to microfluidic cell culture systems in which ECs are either cultured on two-dimensional (2D) surfaces of a microchannel,[14] allowed to self-assemble into microvasculature in hydrogel chambers,[15] or formed upon assembly onto hydrogel-patterned microchannel walls.[16] The latter organotypic vessel-on-chip systems have the advantage of being reproducible and robust

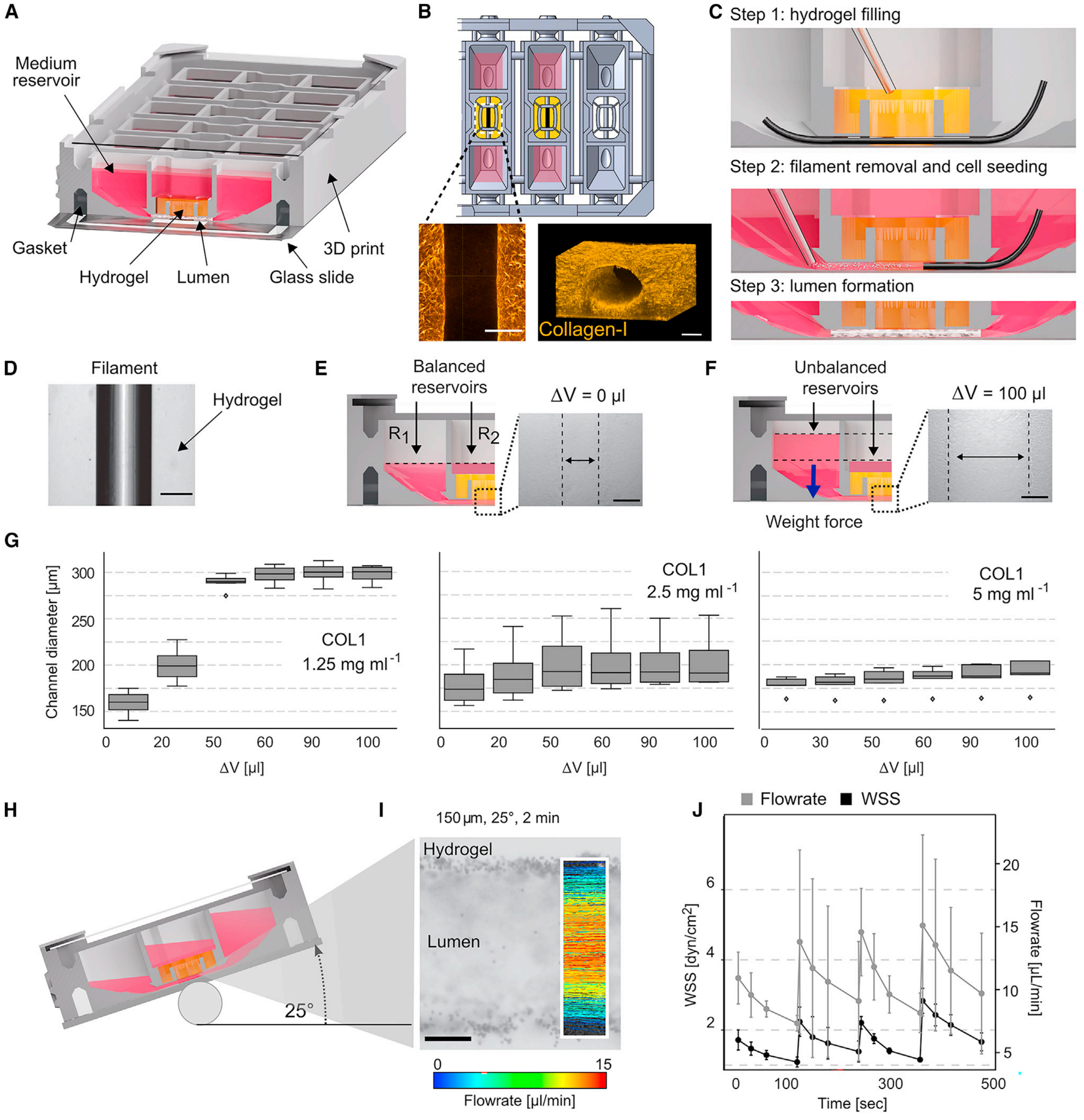

Figure 1. The open microfluidic chip platform for organotypic cell cultures

(A) Cross-sectional view of the 3D-printed chip. The chip holds six identical unit cells, where each unit cell has two reservoirs connected by a hydrogel chamber for tissue culture formation.

(B) Top view of the chip. Zoom-in images show confocal laser reflection images (488 nm) of the collagen I (COL1) hydrogel chamber (5 mg mL^{-1}) with the patterned microfluidic channel. The microchannel runs 100 ± 10 µm above the glass substrate and connects the two fluid reservoirs. Scale bar, 150 µm.

(C) Manufacturing steps of the microchannel. Step 1: a nylon filament is introduced to the chip before filling and polymerization of the hydrogel solution in the middle chamber. Step 2: a cell suspension is pipetted into the reservoirs. Upon mechanical removal of the filament through the reservoir, cells are dragged into the microchannel. Step 3: cells are cultivated and allowed to form tight endothelial structures.

(D) Image of a nylon filament with a diameter of 150 µm in a 2.5-mg mL^{-1} COL1 hydrogel. Scale bar, 100 µm.

(E and F) Images of reservoirs and hydrogel chamber with (E) balanced and (F) unbalanced fluid volume. Within the open microfluidic chip design, the microfluidic channel in the hydrogel widens depending on the hydrostatic pressure acting on the microchannel. Scale bar, 100 µm.

(legend continued on next page)

because microchannel geometry determines the form factor of the vessel size. Like all miniaturized organ-on-chip (OoC) systems, relatively low cell material challenges downstream analytics, whereas larger biochip footprints interfere with standard parallelization and automation. Vessel-on-chip approaches have, to date, mainly used primary or immortalized ECs.[17] Functionally, on-chip vascular disease models have been used to recapitulate the onset of atherosclerosis development, a process that involves the accumulation of lipids, mainly cholesterol-containing low-density lipoproteins (LDLs), in arterial ECs. The subsequent generation of reactive oxygen species (ROS) leads to the formation of vessel lesions, EC dysfunction, impaired vasodilation through reduced nitric oxide (NO) synthesis, flow disturbances, and local inflammation.[18]

We here report the development of a human stem cell-based blood vessel-on-chip model. The open design of the 3D-printed microfluidic chip platform enables multiomics downstream cell analysis with a low sample volume and cell number. Gravity-driven flow on chip induced barrier function, sprouting, and arterial toning of SC-ECs as shown by single-cell transcriptomics and high-resolution imaging. Upon individual stimulation of SC-ECs with oxidized low-density lipoprotein (oxLDL) and free fatty acids (FFAs), early onset of atherosclerosis hallmarks was monitored. Proteomic and secretome changes in the vessel-on-chip system due to oxLDL or FFA stimulation under flow revealed distinctive ROS and NO synthesis responses. Taken together, we provide a fully integrated stem cell-based vessel model for multiomics cell analyses that can readily integrate with epithelial tissues of distinct origins.

RESULTS

Design and characterization of the open OoC platform

The main body of the open OoC platform was produced using 3D stereolithography printing and bonded to an adhesive foil on a glass substrate (Figure 1A). Each chip exhibited six arrayed unit cells, where each unit cell contained a hydrogel chamber and two fluid reservoirs, each holding an adjustable volume between 30 and 150 μL. Relevant chip dimensions are shown in Figure S1A. The gel chamber was connected to the fluid reservoirs using short microfluidic channels with a diameter of 350 μm on each side. Through the connecting channel, a nylon filament with a diameter between 50 and 250 μm can be introduced. The hydrogel chamber was filled with hydrogel prepolymers to encapsulate the nylon filaments. Upon removing the nylon filament through one of the fluid reservoirs, the hydrogel was patterned with a straight microfluidic channel (Figures 1B and 1C). The resulting microchannel width in the hydrogel slightly differed from the nominal diameters of the nylon filaments. However, the microchannels were robustly patterned for nylon filaments with diameters of 50, 150, and 250 μm (Figure S1B). The gel chamber contained a scaffolding structure with four poles connected by a top ring to stabilize the hydrogel over longer culture times. The pole structure is connected to the main body of the chip using rated breakpoints. Upon detaching the pole structure from the main chip body, the hydrogel with the embedded tissue can be retrieved for downstream analytical sample preparation, such as histology. The two outer reservoirs fluidically communicate through the microchannel; thus, the addition of fluids within one reservoir leads to gravity-driven flow and fluid leveling through the communicating channel. However, the two outer fluid reservoirs not only equalize the hydrostatic pressure but the hydrogel chamber also contributes to filling height homeostasis owing to the open microfluidic design. One consequence is that the hydrostatic pressure difference resulting from non-equalized fluid volumes in the reservoirs and hydrogel chamber leads to the dilation of the microfluidic channel because the hydrostatic pressure acts on the gel phase (Figures 1D–1F). The dilation of the microchannel depends on the mechanical properties of the hydrogel. Representatively, we show the dilation of a 150-μm microchannel used by default within a collagen I (COL1) hydrogel with increasing COL1 concentration. While imbalances of fluid filling heights between the reservoir and the gel chamber have a strong effect on the microchannel width in the low-concentrated COL1 hydrogel (1.25 mg mL^{-1}), imbalances of the fluid filling heights within the higher concentrated COL1 hydrogel (5 mg mL^{-1}) have lower effects on the microchannel width (Figure 1G). The chip can be placed on a rocking shaker to induce gravitational flow on it; thus, no active pump system is required to maintain the cell cultures under flow conditions (Figure 1H). To quantify the wall shear stress (WSS), we assessed the flow velocity as a function of the tilt angle of the chip by tracking the motion of microbeads within video frames (Figure 1I and see Star Methods). The determined WSS for a nominal 150-μm channel within 2.5-mg mL^{-1} COL1 hydrogel with tilting angles of 7°/13°/25° are exemplarily shown in Figure S1C. As expected, the WSS increased with higher tilt angles and the flow rates decreased with time because of the leveling of the filling heights between the reservoirs. As the maximum flow rate of 15 μL min^{-1} on chip was achieved at a tilting angle of 25°, this tilting angle was set as the default for all experiments. After tilt initiation, half of the maximum WSS was observed after 2 min (Figure 1J). This time was used as the frequency for changing the tilt direction and maintaining the bidirectional flow. Using three different nylon filaments with diameters of 50, 150, and 250 μm, the effect of the microchannel diameter on the flow rates and WSS was subsequently investigated (Figures S1D and S1E). A maximum volumetric discharge of 15 μL min^{-1} was calculated

(G) Boxplots show the dilation of the microfluidic channel depending on the COL1 concentration and volume differences in the reservoirs and hydrogel chamber. Error bars indicate confidence intervals (CIs) of 95%.

(H) Gravity-driven flow is enabled by tilting the chip platform.

(I) Flow rates within a microchannel with a nominal diameter of 150 μm were determined by video tracking the microbeads. The representative velocity profile within the microchannel is provided for the maximum tilting angle of 25°. Scale bar, 50 μm.

(J) Flow rates on the chip are not constant due to fluid leveling over the reservoirs. The graph shows the time-dependent changes in the flow rates and mean wall shear stress (WSS) inside the microchannel at tilt angles of 25°. The tilting angle was reversed every 2 min to maintain a bidirectional gravity-driven flow. Error bars indicate standard deviation. See also Figure S1.

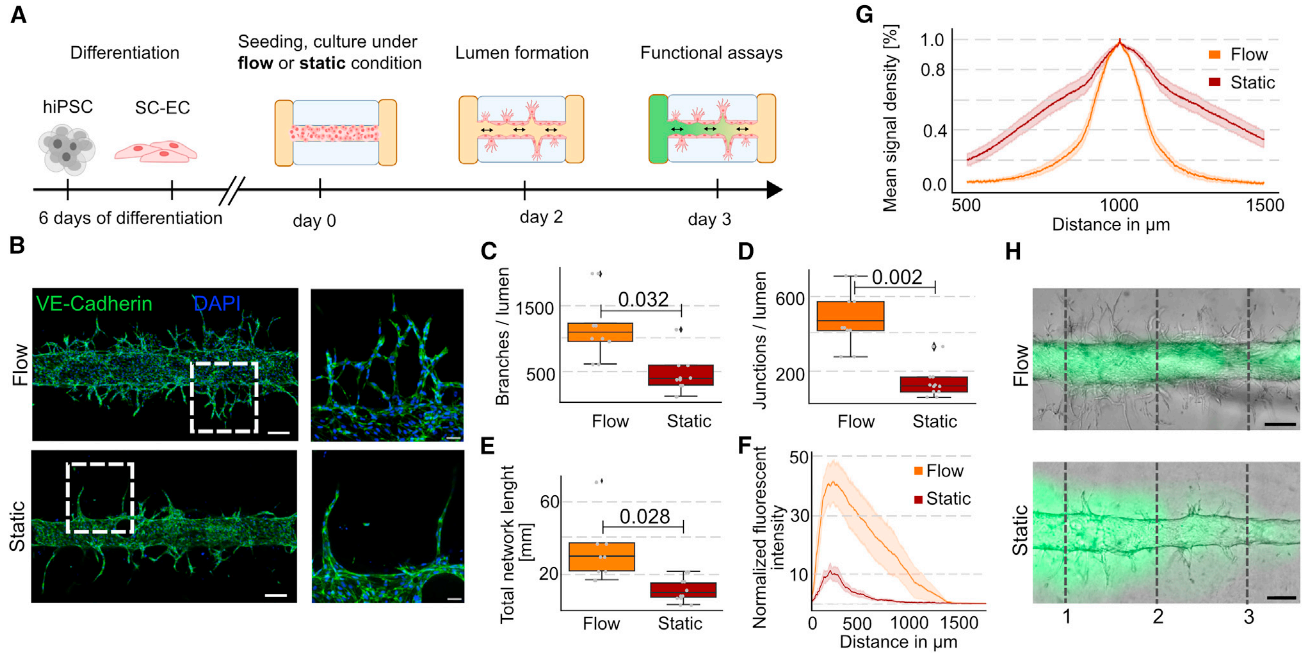

Figure 2. Formation of a functional perfused endothelial vessel-on-chip displaying barrier integrity and sprouting angiogenesis

(A) Experimental outline: stem cell-derived endothelial cells (SC-ECs) are differentiated from human induced pluripotent stem cells (hiPSCs) and seeded in the chip. Functional tests such as *in vitro* vessel integrity test by infusing the lumen with fluorescently labeled fluorescein isothiocyanate (FITC)-dextran are performed after 2 days.

(B) IF images of vascular endothelial (VE)-cadherin (EC contact integrity) of 2-day cultured SC-ECs under bidirectional flow or static conditions on chip. Scale bar, 200 μm left and 100 μm right.

(C–E) Sprouting network analysis of the SC-ECs under bidirectional flow and static conditions showing branches (C) and junctions (D) per lumen and total vascular network length (E); n = 6 from two independent experiments; *p* values are calculated using a parametric two-sided t test and indicated in the figure; error bars indicate 95% CI.

(F) Sprout density was measured using the mean intensity of the VE-cadherin signal on multiple longitudinal axes directing from the outer wall of the microchannel toward the hydrogel area (n = 6 of two independent experiments, CI = 68%).

(G) FITC-dextran assay to evaluate the barrier function of SC-EC vessels. The mean fluorescence intensity signal of FITC-dextran was measured on three traverse lines scans per lumen (dotted lines in H; n = 8 of three independent experiments, CI = 68%).

(H) Images are fluorescence and brightfield overlays, where green denotes the FITC-dextran signal. Scale bar, 200 μm. See also Figure S2.

at 150-μm diameter in the center of the microchannel at a 25° tilt (Figure S1D). Increased microchannel diameters resulted in a greater maximum WSS but a faster reduction in WSS over time (Figure S1E). Microchannel diameters of 150 and 250 μm produced shear forces in the range of 1–3 dyn cm^{-2}, whereas a microchannel diameter of 50 μm produced negligible shear forces. In the following experiments, we use only chips with a 150-μm diameter and a maximum tilt of 25° inducing a shear force of 3 dyn cm^{-2}, which is at the lower end of the shear force microvessel experience *in vivo*.[19]

Formation of the functional perfused endothelial vessel on chip

Next, we applied the chip for the formation of SC-EC *in vitro* vessel structures. Using a two-step induction protocol for ECs, hiPSCs were differentiated in 3D shaking culture.[8] SC-ECs were expanded and seeded at high density (4 million cells mL^{-1}) into the chip with a pre-formed microchannel in a 2.5-mg mL^{-1} COL1 hydrogel (Figure 2A). The cells began to adhere to the channel walls within the first hour. Within the following 2 days, cells were cultivated under either static or bidirectional flow conditions. In both cases, SC-ECs formed a luminal vessel structure adopting the shape of the microchannel, with sprouts developing toward the hydrogel periphery after 2 days of cultivation (Figures 2B and S2A).

We analyzed the sprouting network parameters within 3D-stacked confocal images in which VE-cadherin was immunohistochemically stained to quantify the differences in endothelial sprouting capability under static or flow conditions (Figure S2B). Notably, SC-ECs under flow conditions formed more branches protruding from the lumen in terms of the total number, junctions per branch, and total network length (Figures 2C–2E) than under static conditions. This higher sprouting behavior was further confirmed by fluorescence signal analysis using VE-cadherin staining (Figure 2F). The VE-cadherin signal along the perpendicular axis of the microchannel showed a higher amplitude and length, which represented a higher number and longer sprouts within the samples cultured under flow conditions.

Sprouting analysis indicated that ECs interacted with the extracellular matrix (ECM) and started to remodel the surrounding hydrogel via sprouting angiogenesis. COL1 is one of the most abundant ECM proteins and is a favorable hydrogel for constructing

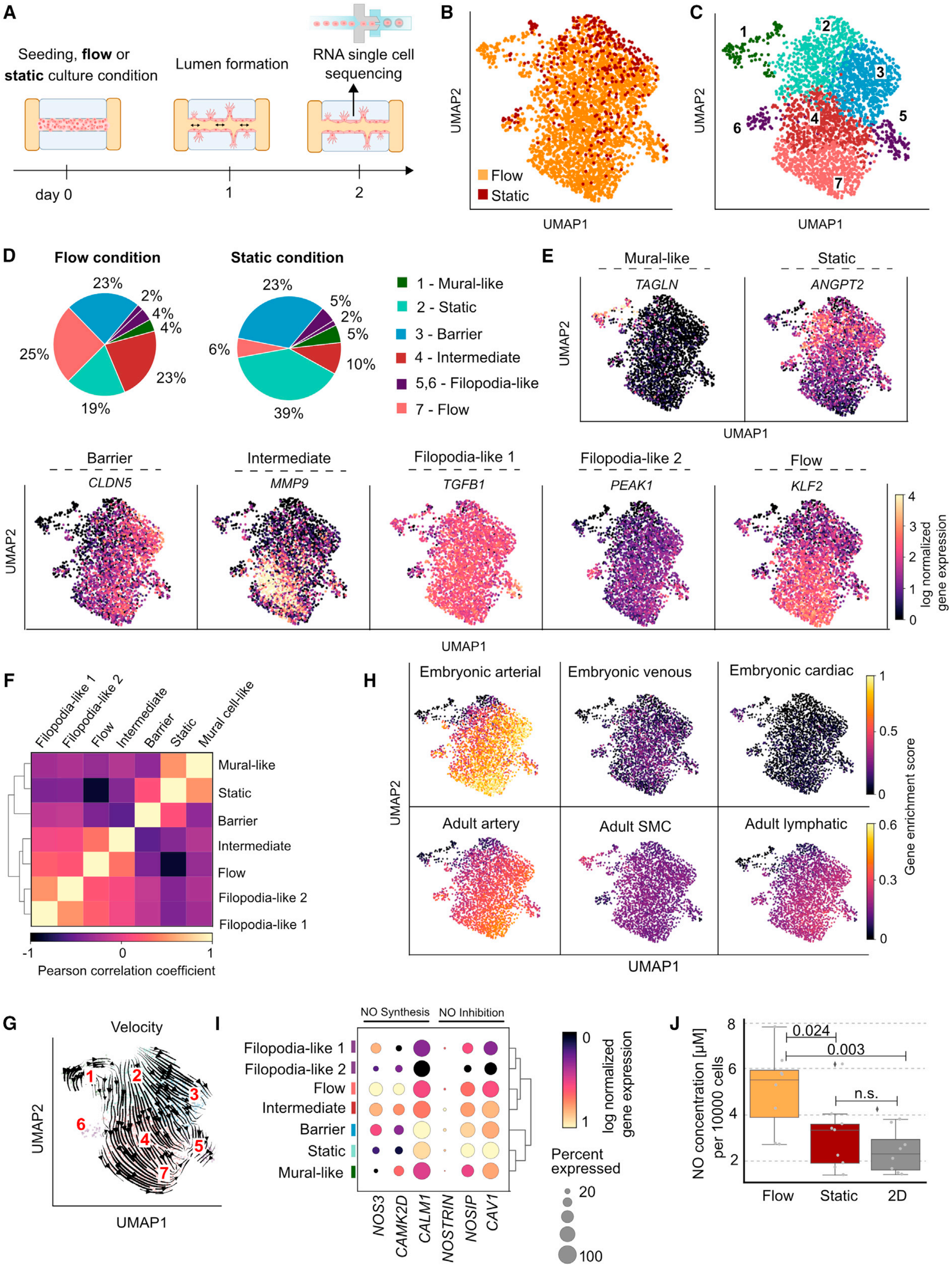

(legend on next page)

in vitro blood vessels.[20] We demonstrated the extent to which the hydrogel formula influenced cellular hydrogel remodeling and sprouting by seeding SC-ECs on a chip at different COL1 concentrations. At the lowest COL1 concentration (1.25 mg mL^{-1}), the cells visibly remodeled the microchannel by sprouting out of the lumen toward the ECM periphery, leading to significant lumen enlargement. By contrast, at higher concentrations (2.5 and 5 mg mL^{-1}), the lumen diameter was less impaired (Figure S2C). At a collagen concentration of 5 mg mL^{-1}, only a few sprout tips were observed. This suggests that denser collagen networks promote lumen stability while impeding the growth of the SC-EC branches. Hereafter, all experiments were performed with a COL1 concentration of 2.5 mg mL^{-1} to maintain the lumen structure and sprouting capability of the SC-ECs. A fluorescein isothiocyanate (FITC)-dextran assay was performed to test the barrier function of the endothelial lumen. The SC-EC lumen engineered under flow conditions showed higher resistance to FITC-dextran diffusion (40 and 2,000 kDa) over the endothelial barrier into the COL1 hydrogel matrix than the SC-EC lumen engineered under static conditions over 3 days (Figures 2G, 2H, S2D, and S2E).

Single-cell transcriptomic and functional analysis of the SC-EC on chip

Next, we performed single-cell transcriptomic analysis (single-cell RNA sequencing [scRNA-seq]) of SC-ECs cultured on chip under shear flow and static conditions to reveal the heterogeneity of cell stages associated with possible maturation, sprouting, or barrier function (Figure 3A). We obtained sufficient SC-ECs for the scRNA-seq protocol by pooling the SC-ECs from one chip, which are six functional lumens with approximately 3,000 cells each. The live cell recovery rates from the chip were >70% for SC-ECs cultured under flow conditions, demonstrating that the retrieval process was robust. For SC-ECs cultured under static conditions, the live cell recovery rates were lower, indicating a lower viability or higher stress state of these cells (Figures S3A and S3B). Cells retrieved from the chip were used as inputs for scRNA-seq. The quality parameters of the sequencing run are shown in Figures S3C–S3G. After high-quality scRNA-seq data filtering, we obtained single-cell transcriptomes of >17,000 genes from approximately 2,000 cells (Figure S3D) under both conditions. Seven cell clusters were identified using Leiden[21] clustering (resolution = 0.5) and 2D data reduction (UMAP[22]) of the single-cell transcriptome data (Figure S4A). The Leiden clusters were annotated as flow, static, intermediate, barrier, filopodia-like 1/2, and mural cell-like transcriptomic states based on the marker genes (Figure 3B, 3C, 3E, S4B, and S4C). Notably, only the mural cell-like cell cluster did not express the EC markers and showed typical vascular smooth muscle cell marker expression, including that of *PDGFRB*, *CSPG4*, *TAGLN*, and *ACTA2*.[23] We and others have previously shown that ECs and mural-like cells co-evolve during the applied stem cell differentiation protocol[8,24] and that progenitors are still present on day 6 of differentiation. A low fraction of mural-like cells may have resulted from incomplete sorting. The differentially expressed genes (DEGs) for SC-ECs cultured under static conditions included the EC markers, such as *EDN1* or *ANGPT2*, which are specific for static SC-EC culture conditions since shear flow stress leads to their downregulation.[13,25] Furthermore, cells from the static cell cluster shared the expression of stress marker genes, including *ROMO1* and *NQO1*, indicating oxidative stress and cell death.[26] Contrastingly, only 19% of the single-cell reads found in the SC-ECs exposed to WSS were allocated to the static cluster, whereas 39% of the statically cultured SC-ECs were allocated to the static cluster (Figure 3D). SC-EC distribution cultured under flow and static conditions within annotated cell clusters is shown in Figure 3D. Under flow-culture conditions, half the SC-EC population exhibited transcriptomic states of either intermediate (23%) or flow (25%) cell clusters. Furthermore, cells from the flow cluster showed upregulated expression of shear stress markers, including *KLF2*, *KLF4*,[13] or *VWF*.[27] Notably, *GJA4* is a shear stress-upregulated gene and enables arterial specification together with the downstream cell cycle inhibitor *CDKN1B*,[28] which is also specifically upregulated in the flow cell cluster. This aligns with *MECOM* upregulation in the flow cluster, a regulator of human arterial gene expression.[24]

Intermediate clustered cells upregulated the expression of *MMP9*, which is a shear-stress-sensitive gene[29] and central for the initiation of angiogenesis in the endothelial progenitors.[30] Cells of the intermediate cluster also express the pro-oncogene *JUN*, which is upregulated in the ECs as an immediate response to shear stress.[31] Approximately 7% of the SC-ECs in both static and flow-culture conditions were assigned to one of two filopodia-like transcriptomic cell states. Filopodia cluster 1 was

Figure 3. Single-cell transcriptomics reveal specified flow-induced cell clusters reflected by enhanced NO synthesis in *in vitro* conditions

(A) Experimental outline: SC-ECs cultured for 2 days under bidirectional flow or static culture conditions on chip. Cells were retrieved from the chip and used for 10X Genomics scRNA-seq.

(B) Uniform manifold approximation and projection (UMAP) plot of the two acquired single-cell transcriptomic datasets.

(C) UMAP plot illustrating the seven unique found transcriptomic cell clusters for the SC-ECs cultured on chip.

(D) Cell distribution according to the identified cell clusters.

(E) Gene expression patterns of the selected cell marker genes used for cell cluster assignments.

(F) Pearson correlation plot of the annotated cell clusters.

(G) Single-cell transcriptomic velocity analysis. Velocity streamlines showed the transcriptomic state progression of SC-ECs cultured for 2 days under bidirectional flow on chip.

(H) Enrichment score of DEGs from embryonic arterial, venous, and cardiac ECs (human embryonic dataset at Carnegie stage 10 and 11) and of adult artery ECs, smooth muscle cells, and adult lymphatic ECs (Tabula Sapiens organ-type vasculature dataset) within the on-chip scRNA dataset.

(I) Dot plots show expression levels of genes required for endothelial NO synthesis and inhibition of the NO synthesis.

(J) NO concentrations within the luminal cell culture media of the chip from cells cultured under flow or static conditions. NO concentrations are compared to supernatants of cells grown on a 2D monolayer (n = 8–9 from 3 independent experiments; error bars indicate 95% CI). NO concentrations were normalized to the total cell count per sample. *p* values were calculated with a parametric one-way ANOVA and Tukey's *post hoc* test and are indicated in the figure. See also Figures S3 and S4.

positive for vascular endothelial growth factor (VEGF)/calcium signaling, and filopodia cluster 2 was correlated with NOTCH and ECM-receptor interaction as revealed by a Kyoto Encyclopedia of Genes and Genomes (KEGG) pathway analysis (Figure S4C). A representative selected DEG for filopodia cluster 1 was transforming growth factor β 1 (*TGFB1*), which is known to induce angiogenesis.[32] In addition, *PEAK1* was chosen as unique marker for filopodia-like 2.[33] SC-ECs within the barrier cluster upregulated the expression of cell-cell interaction genes (*CLDN5* and *ENG*) as well as gap and tight junction genes (*GJA1* or *JAM3*), which indicated the formation of a cell-cell interaction required for intact lumens.[32,34] Cells from static and flow-culture conditions were found in the barrier cluster, suggesting that the prepatterned luminal shape of the hydrogel alone was sufficient for the formation of the transcriptomic cell state. KEGG pathway analysis and Pearson correlation plots supported the annotation and differences in all transcriptomic states, respectively (Figures 3F and S4C).

RNA velocity[33] was calculated using the scRNA-seq flow data to resolve the dynamic changes and interconnectivity of cell clusters (Figure 3G). The flow velocity lines point from the static cluster toward the intermediate, barrier, flow, and filopodia-like clusters. Next, we investigated whether the velocity lines indicated SC-EC maturation under flow-culture conditions. To this end, we calculated the gene enrichment scores for DEGs obtained from embryonal and adult human endothelial single-cell datasets within the SC-EC single-cell transcriptome data. Strikingly, the DEGs of the embryonic early arterial (Carnegie stage 10 and 11)[35] and the adult artery ECs (human scRNA atlas)[36] considerably increased along the velocity lines (Figure 3H), thus supporting the maturation effect of SC-ECs under shear-flow-culture conditions. The gene enrichment score for DEGs of adult lymphatic ECs also increased within SC-ECs cultured under shear flow conditions, but to a lower degree, arguing that the on-chip conditions drive cell type maturation toward an arterial-like cell type. Similarly, cells of the mural cell cluster correlated with the transcriptomes assigned to the adult smooth muscle cells. Contrarily, the enrichment analysis showed that SC-ECs on chip did not resemble embryonic cardiac ECs.

Moreover, in the flow, intermediate, barrier, or filopodia clusters, the expression profile of ECM proteins changed compared to cells cultured under static conditions (Figure S4D). For example, barrier cells increased the expression of the basal membrane protein collagen IV, also found by IF-stained lumen sections (Figure S4E).

Shear stress is known to be a positive regulator of endothelial NO synthesis.[25] Genes involved in NO signaling belonged to the DEG of the single-cell flow clusters. Vascular cells synthesize NO to maintain healthy tissue function and to control vasodilation.[37] Endothelial NO synthase (eNOS/*NOS3*) and the NOS3-activating Ca-dependent protein kinase (*CAMK2D*) are upregulated in ECs cultured under flow conditions.[38] Contrastingly, under static cell culture conditions, ECs upregulated genes, such as eNOS-interacting proteins (*NOSIP*), eNOS traffic inducer (*NOSTRIN*), and Caveolin-1 (*CAV1*), which form a ternary complex inhibiting NOS3 activity[37] (Figure 3I). We determined NO concentrations in the supernatants of the perfused lumens cultured under flow and static conditions using a fluorometric assay to validate the gene expression changes at the functional level. Indeed, NO production was significantly increased in the ECs cultured under flow conditions, whereas NO concentrations in the ECs cultured under static conditions were comparable to those in cells grown in a 2D monolayer (Figure 3J).

Interfacing the vessel-on-chip platform for downstream analysis

The open OoC platform was designed to enable high-resolution imaging. A working distance of 100 μm between the microchannel and the glass substrate allowed whole-mount imaging of the SC-EC vessel structure (Figure 4A). Therefore, immunofluorescence (IF) staining can be performed with a low antibody consumption. A z-projection of fluorescence confocal images depicting SC-EC lumen stained for the endothelial marker CD31 is shown (Figure 4B) and a 3D reconstruction of the image stack visualizes the distribution of SC-ECs in the lumen (Video S1). Additionally, we stained for the sprouting marker DLL4 and lamellipodia marker ARP3. Lamellipodia appeared at plasma membrane sites free of VE-cadherin as reported before,[39] and ARP3 expression was observed in the cell membrane regions next to newly found sprouts. Alternatively to the whole-mount staining, sample sections can be prepared for multiple protein detections in a single lumen. For this, the COL1 hydrogel was retrieved in an unscathed manner by lifting the hydrogel-embedded 3D-printed support structures (Figure 4C). Hydrogel blocks with intact lumens were then subsequently used for downstream histological analyses. Representative IF-stained sections are shown in Figure 4D, where we stained selected DEGs, such as angiopoietin-2, claudin 5, and KLF4, found in the scRNA-seq dataset. Approximately 25 sections were obtained from each lumen.

Modeling the early onset of atherosclerosis by oxidative stress under *in vitro* conditions on chip

Elevated blood levels of oxLDL and FFA are crucial drivers of atherosclerosis plaque formation.[40,41] To model the early onset of atherosclerosis on chip, we treated SC-EC vessels under flow conditions with either FFA or oxLDL (Figure 5A) for 48 h. Both FFAs and oxLDL accumulated within the SC-ECs, which was verified using BODIPY staining for all cytoplasmic lipids or using fluorescently labeled Dil-oxLDL (Figures 5C and 5D). An FITC-dextran membrane-permeability assay was performed to assess the barrier function of the vessels-on-chip after 24- and 48-h oxLDL and FFA treatment. While vessels treated with FFA showed no difference in barrier function, vessels treated longer than 24 h with oxLDL indicated a small increase in FITC-dextran leakage (Figures S5A and S5B). Further, IF stainings showed that the expression pattern of ZO1 changed from a plasma membrane to a cytoplasmic location in SC-ECs after 2 days of oxLDL treatment but not after FFA treatment or in control samples (Figure S5C). A cytoplasmatic location of ZO-1 has been reported upon hypoxia stress induction in ECs.[42]

The stimulation responses of SC-ECs were quantified by measuring the proteomic changes using liquid chromatography-tandem mass spectrometry (LC-MS/MS). Cells from the three lumens were retrieved and pooled to obtain approximately 9,000 cells. Protein counts and the dynamic range of proteomic

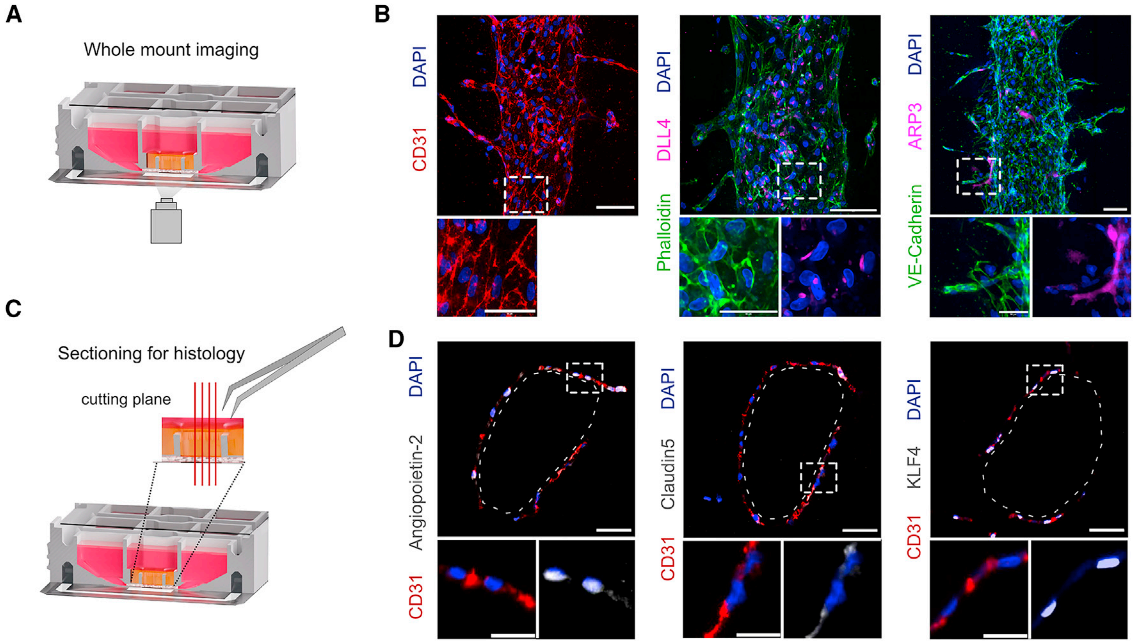

Figure 4. Whole-mount and paraffin-section IF staining allow for detailed morphological analysis of endothelial tissue

(A) On-chip whole-mount IF staining can be directly performed where, concomitantly, the 100-μm distance of the lumen to the glass bottom allows high-resolution imaging.

(B) Whole-mount staining of DEGs expressed in SC-ECs cultivated under bidirectional flow on chip. EC marker CD31 (scale bar, 100 μm), flow-induced marker DLL4 (scale bar, 50 μm), endothelial adherence junction marker CDH5, and branching marker ACTR3 (scale bar, 50 μm) with zoom-in images (scale bar, 20 μm).

(C) For performing multiple IF staining from a single sample, the printed scaffold with the hydrogel-embedded vessels is removed using a tweezer.

(D) Stainings of static cell marker ANPT2, barrier marker CLDN5, and flow-induced marker KLF4. Scale bars, 50 μm and 20 μm for the zoom-in images. See also Video S1.

data were comparable for all samples (Figures S6A–S6C). FFA formulation required BSA in the medium and thus the buffer conditions between the samples differed. Principal-component analysis and heatmaps showed differences in protein expression between the treatments and respective media controls, as well as coherence between repeats (Figures 5B, S6D, and S6E). Differentially expressed proteins (DEPs) from both stimulation experiments were resolved using volcano plots (Figures S6F and S6G). Gene Ontology (GO) term analysis of the DEPs from both treatments showed enrichment of oxidative stress terms and included terms indicating the activation of protective oxidative reagents via the heme-oxygenase system[43] (Figures 5E and 5F). GO terms for the FFA-treated samples included additional terms related to shunting overload of fatty acid activity or obesity-related inflammation, e.g., by the upregulation of toll-like receptor 4 (TLR4) signaling.[44] DEPs found within both treatments and unique to a treatment are shown in the Venn diagram in Figure 5G. Both treatments led to the upregulation of heme oxygenase 1 (HMOX1), which is expressed as a protective response to ROS stress.[45] We live-stained the SC-ECs on chip with a fluorescence indicator (CellROX) for ROS species to test whether oxidative stress was induced by FFA and oxLDL treatment. The normalized mean intensity signal of the CellROX fluorophore (Figure 5H) increased in oxLDL-treated SC-ECs with a signal intensity comparable to that of the positive control treatment of the cells with *tert*-butyl hydroperoxide (TBHP). For FFA treatment, we did not detect an increase in the CellROX signal compared with the respective medium control.

Next, we investigated whether adding the sortilin inhibitor TY52156 could lower oxidative stress in SC-ECs. Proteomic analysis showed that a sortilin family member (SORCS2) was upregulated in SC-ECs upon FFA (1.56-fold; adjusted p = 0.03) and oxLDL (1.40-fold; p = 0.02) treatment. Sortilin was previously found to be positively correlated with atherosclerosis and cardiovascular disease.[46] TY52156 co-treatment did not lead to a visibly altered FFA or oxLDL accumulation (Figure S6H). Notably, in the oxLDL + TY52156-treated samples, the CellROX signal was significantly lower than that in the samples treated with oxLDL alone (Figure 5H). In the FFA-treated SC-ECs, TY52156 had no significant influence on CellROX signaling.

Considering the enrichment of proteins related to eNOS function (ENG, CYBG, and HMOX1) in the proteome analysis of both conditions we quantitatively measured NO production by SC-ECs on an OoC after oxLDL and FFA treatments. Indeed, NO concentrations in the oxLDL-treated SC-EC vessels were significantly reduced compared to those in the respective medium controls (Figure 5I). Here, the sortilin inhibitor TY52156, applied to oxLDL-treated SC-ECs, did not rescue the NO production. The NO assay on the FFA-treated samples did not show any difference compared to the medium control, which aligns with the non-significant CellROX staining. Thus, when compared to

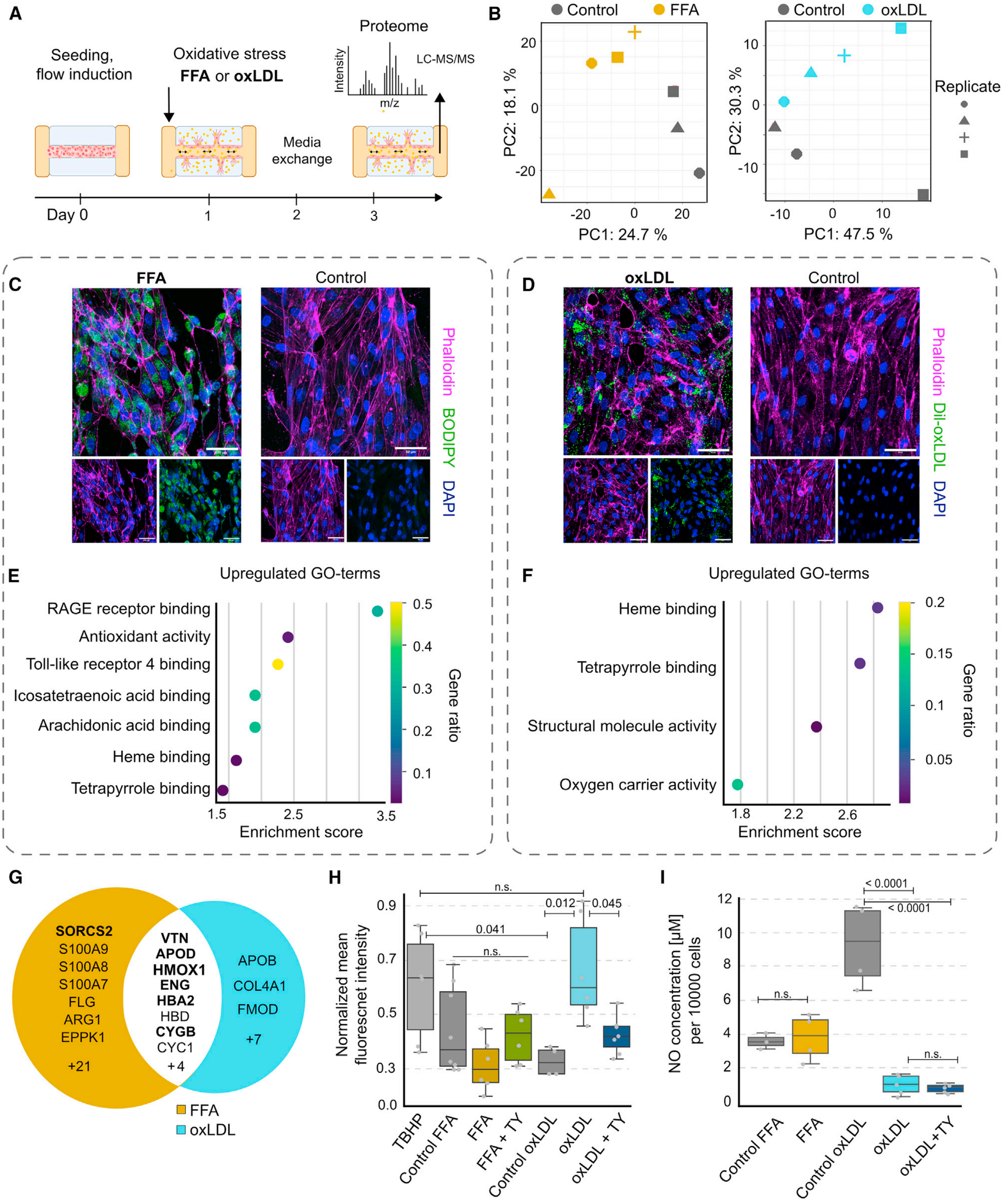

Figure 5. Oxidative stress induction of vessel formed on chip

(A) Experimental outline. On day 1, SC-ECs were treated with free fatty acids (FFAs) or oxidized LDL (oxLDL). On day 3, proteome and secretome data were acquired using mass spectrometry.

(B) Principal-component analysis of the proteome data after FFA (n = 4) or oxLDL (n = 4) treatment and their respective medium controls (n = 3).

(legend continued on next page)

oxLDL, SC-EC treatment with FFA leads to different molecular response mechanisms.

To further investigate the oxidative stress response of the SC-ECs, we measured the secretome of the cells. For this purpose, we used the flow-through volume in the reservoirs of the chip for LC-MS/MS analysis (Figure 6A). There were 1,939 secreted proteins with high confidence level, retrieved over a time interval of 24 h from SC-ECs treated with oxLDL, identified by mass spectrometry, and 152 proteins of the secretome were up- or downregulated by a 1.5-fold change in comparison to the control, from which 45 contained a signal peptide for active secretion into the blood.[47] A GO term analysis of DEPs of the secretome with active secretion signals showed enrichment of proteins for high-density lipoprotein (HDL) and chylomicron remodeling (Figure 6B). Among the upregulated proteins in the secretome were members of the apolipoprotein family (Figure 6C). For example, the secreted APOC3 and APOA1 are known to change NO synthesis of ECs and are linked to pathophysiological processes leading to cardiovascular disease (CVD).

Within the secretome of SC-ECs treated with FFA, 693 proteins were determined, where only 18 were differentially regulated in comparison to the control sample (Figure 6B). SC-EC secretomes in response to FFA and oxLDL treatment have no overlap, showing once more the differently induced stress. Notably, in agreement with the proteome measurements, the FFA treatment led to an increased secretion of the SORCS2 (Figure 6D).

DISCUSSION

In this study, we manufactured an open microfluidic platform for engineering organotypic endothelial vessel structures. The open microfluidic design enables the platform to interface with all state-of-the-art analytical technologies, including scRNA-seq, proteomics by LC-MS, and high-resolution imaging. Concomitantly, engineered endothelial tissues can be functionally assessed under mechanical- and fluid-controlled culture conditions. The manufacturing of the chip platform was robust, as validated by more than 500 lumens in the presented dataset. Although we only functionally analyzed lumens using COL1 hydrogels, microchannel formation was also positively confirmed for Matrigel or fibrin hydrogels (data not shown), in support of general applicability of our OoC platform for all commonly used tissue microenvironments.

Upon on-chip adjustment, our gravity-driven flow-culture microenvironment revealed WSS of up to 3 dyn cm^{-2}. This value correlates with physiological flow in microcapillaries but unsurprisingly remains lower compared to flow in larger vessels.[19] Generated on a rock shaker and hence bidirectional, the functional validation that our SC-derived EC vessel structures recapitulate vascular barrier integrity or physiological process as sprouting.

We previously resolved the transcriptomic trajectory of SC-ECs during microvessel formation in a hydrogel microenvironment.[8] In this study, we used the same SC-ECs for the luminal vessel structure. Single-cell transcriptomic data, particularly velocity analysis, revealed dynamic cell-state changes of SC-ECs from static to flow-culture conditions. Live/dead staining of SC-ECs on the chip under flow and static conditions revealed no differences (Figure S3A); however, SC-EC retrieval from the on-chip static culture condition resulted in a higher dead cell count, suggesting generally lower cell stress of SC-ECs under flow-culture conditions. This is probably related to the expression of stress-related genes such as *NQO1* or *ROMO1*,[26] especially in the "static" cluster. Notably, the resolved SC-EC cell states were in accordance with the morphological and functional phenotypes of the chip, including sprouting, barrier-forming, and flow-exposed ECs. SC-ECs under shear flow upregulated the shear-stress-responsive genes essential for vascular function, including *KLF2*/*KLF4* under flow conditions.[48] Most strikingly, the higher transcriptomic correlation of the SC-ECs cultured under flow-culture conditions with adult arterial ECs demonstrated the flow maturing effect on the SC-ECs. Staining for endothelial markers (CD31), sprouting markers (DLL4 and ARP3[39]), static marker (ANGPT2[13]), barrier marker (CLDN5[32]), and flow induction marker (KLF4[13]) substantiated the single-cell transcriptomic data at the protein level, and hence the translation into biological function.

Another central finding derived from our vessel-on-chip model is the identified transcriptomic upregulation of NO synthesis, respective signaling genes, such as eNOS (*NOS3*) and *CAMK2D*, under flow-culture conditions. In stark contrast, SC-ECs cultured under static conditions revealed increased expression of genes known to downregulate eNOS function, e.g., *NOSTRIN*, *NOSIP*, and *CAV1*.[37] An on-chip quantitative assay (Figure 3J) indeed verified the opposing effects of shear versus static culture conditions on NO synthesis and, by extension, on the *in vivo* EC behavior.[49]

Beyond the characterization of the organotypic EC culture on chip, we validated the general functional relevance of the chip platform by modeling the pathogenesis of atherosclerosis. Given that oxLDL particles are involved in the induction of the early characteristic events of atherosclerosis[50] and excess FFAs are present in patients with atherosclerosis, we treated

(C) Immunofluorescent images of fatty acids with BODIPY in FFA-treated samples vs. control. Scale bar, 50 μm.

(D) Immunofluorescent images of fluorescence labeled Dil-ox-LDL-treated samples vs. control. Scale bar, 50 μm.

(E) Top eight upregulated Gene Ontology (GO) terms in the FFA condition compared to the untreated control.

(F) Top four upregulated GO terms in the ox-LDL condition compared to the untreated control.

(G) The Venn diagram highlights the selected proteins upregulated in the FFA and oxLDL conditions and their overlap.

(H) Analysis of the ROS in the treated samples versus control. Samples were live-stained for Hoechst and CellROX reagent (Thermo) and imaged, and the CellRox signal intensity was normalized to the Hoechst intensity. ECs were treated with TBHP as a positive control. Data are presented with 95% CI for the error bars, and $n \geq 12$, except for TBHP with $n = 3$. Boxplot outliers were removed when indicated in the Python package seaborn.

(I) Cell-count-normalized NO concentration (μM) in supernatants of treated samples vs. their respective control on day 3. Error bars indicate 95% CI, and n = 3–5. *p* values of (H) and (I) were calculated with a parametric one-way ANOVA and Tukey's *post hoc* test and are indicated in the figures. See also Figures S5 and S6.

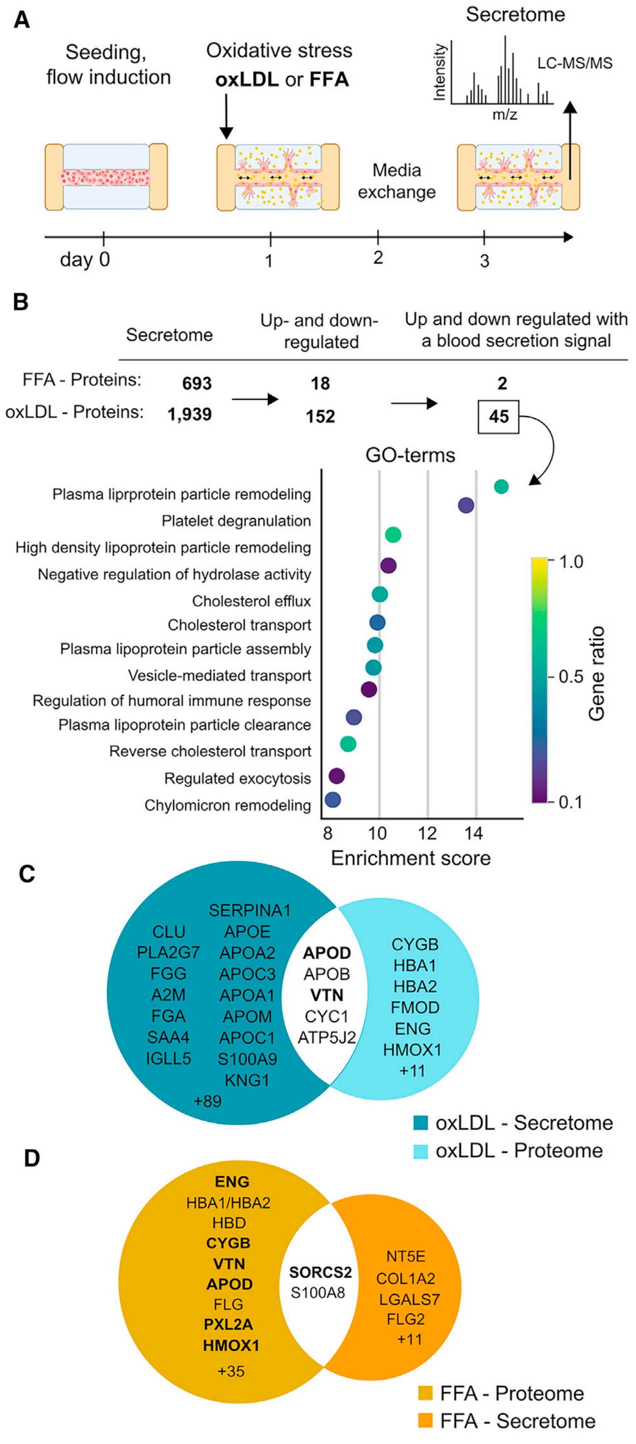

Figure 6. Secretome analysis of oxLDL- and FFA-treated SC-ECs on chip

(A) Experimental outline: SC-ECs were treated with oxLDL and FFA on day 1. Supernatants were collected from the chip reservoirs on day 3 for an LC-MS/MS analysis.

(B) oxLDL treatment resulted in up- and downregulation of secreted proteins with and without export signal compared to a control sample without cells. GO term analysis of the differentially secreted proteins with blood secretion signal revealed a response of the cholesterol metabolism to the oxLDL treatment.

(C and D) Venn diagrams highlight proteins upregulated in the secretome and matched proteome of SC-EC treated by (C) oxLDL and (D) FFA.

our SC-ECs with FFA or oxLDL to potentially address FFA pathomechanisms.[41] One hallmark of oxLDL is the uncoupling of NO production in the ECs via eNOS inactivation.[40] Functional changes, high ROS production, and reduced NO synthesis were indeed observed in the SC-EC vessels-on-chip. The proteome of SC-ECs under oxLDL treatment reflected the ROS-induction, ER-stress, and antioxidant-stress responses. Particularly, the DEPs ENG,[51] CYBG,[52] and HMOX1[45] are known regulators of endothelial NO synthesis and mechanistically link induced ROS with the functional phenotype of reduced NO synthesis. Notably, the increased ROS occurrence upon oxLDL treatment was ameliorated in SC-ECs by adding the sortilin inhibitor TY52156. However, TY52156 did not rescue NO production, indicating either that the ROS-reducing effect of TY52156 could not compensate for NO synthesis or that both responses are not directly interlinked.

Additionally, FFA treatment induced a proteomic stress signature in SC-ECs with overlapping DEPs in response to oxLDL stress. In contrast to the oxLDL treatment and to *in vivo* experimental data, NO production and ROS concentrations were not altered compared to the controls. One explanation for this finding can be the relatively short treatment of 48 h. FFAs are stored in the SC-ECs in small lipid droplets as shown by the BODIPY staining (Figure 5C). Comparably to *in vivo* conditions, endothelium initially buffers excessive FFA loads by storing them in lipid vesicles and degrading those lipids by lipolysis.[53] Therefore, long-term *in vitro* studies are required to answer this question. Notably, an immediate ROS-protective response was initiated through the upregulation of the heme-oxygenase system for both treatments. Vitronectin was an additional upregulated DEP after oxLDL and FFA treatments. Evidently, vitronectin is central to atherosclerosis progression.[54] Elevated vitronectin levels have been suggested as a potent biomarker of coronary artery disease.[55] Vitronectin detection within the secretome after oxLDL treatment underpins the relevance and applicability of the chip for biomarker discovery.

In summary, we developed a robust and easy-to-use open OoC platform for screening parallel endothelial functions using standard laboratory equipment. The reported integration of stem cell-derived ECs offers the opportunity to study *in vitro* endothelial development, tissue-specific toning, and immune interactions at high resolution and at single-cell levels. Beyond the increasing number of vessel-on-chip platforms, our open and general design of the chip allows it to host seamlessly any epithelial cell type. Combined with the open hydrogel design, our setup facilitates the engineering of more complex and particularly vascularized tissues in a "plug-and-play" manner. More broadly, our platform opens avenues for universal use to engineer larger and complex tissue/organs considering the integration of gene-editing tools or patient-specific stem cell lines. Our approach thus serves the urgent need to replace animal models/reduce animal use by developing a functionally reliable and easily customizable vascularized human OoC platform.

Limitation of the study

One limitation of our study is the bidirectional laminar flow profile at a lower WSS regime of up to 3 dyn/cm^2 on the vessel-on-chip platform. Under physiological conditions, blood flow occurs unidirectional, where the WSSs vary, largely depending on organ function, vessel size, or viscoelastic parameters of the blood. For example, shear rates in capillaries or lymphatic vessel range are in the order of 2 dyn/cm^2, whereas in larger arteries the shear stress ranges from 10 to as high as 70 dyn/cm^2.[56] Engineering *in vitro* tissue models on chip is a balance between simplicity in terms of cost-effective handling and screening versus the complexity of the *in vivo* tissue. The presented vessel-on-chip platform provided a dynamic microenvironment in which the SC-ECs established a complete endothelial barrier function, matured to arterial-like ECs, showed NO-secretion comparable to *in vivo* vessels, and enabled higher-throughput screening. On the other hand, under perturbed flow, which is defined as turbulent flow at low shear stress, arteriosclerosis is promoted under *in vivo* conditions. To which extent the bidirectional flow on chip, but also long-term treatments with oxLDL or FFA, contribute to the atherosclerosis model remains to be resolved. From a future perspective, unidirectional flow and higher WSS can be established on our chip by adopting gravity-flow concepts developed for closed[57] microfluidic channel networks, increasing the hydrodynamic flow pressure by increasing the volume of the fluid reservoirs, or the tilt angle of the chip.

STAR★METHODS

Detailed methods are provided in the online version of this paper and include the following:

- KEY RESOURCES TABLE
- RESOURCE AVAILABILITY
  - ○ Lead contact
  - ○ Materials availability
  - ○ Data and code availability
- EXPERIMENTAL MODEL AND STUDY PARTICIPANT DETAILS
- METHOD DETAILS
  - ○ Generation and cultivation of SC-ECs
  - ○ Cryopreservation and passaging of SC-ECs
  - ○ Chip manufacturing
  - ○ Flow characterization
  - ○ Cell seeding on chip
  - ○ Whole mount immunofluorescence staining
  - ○ Histology of lumen sections
  - ○ Confocal imaging
  - ○ Lumen permeability analysis
  - ○ Branching characterization and branch density analysis
  - ○ Live dead cell analysis
  - ○ NO assay
  - ○ Sample preparation for scRNA-seq
  - ○ Pre-processing of scRNA-seq data
  - ○ Clustering and cell type annotation
  - ○ RNA velocity using basic modeling
  - ○ Cell treatment for oxidative stress induction
  - ○ Sample preparation and mass spectrometry measurements
  - ○ Data processing - protein identification
  - ○ Data processing - Label-free quantification
  - ○ Data analysis
  - ○ Oxidative stress compound staining
- QUANTIFICATION AND STATISTICAL ANALYSIS

SUPPLEMENTAL INFORMATION

Supplemental information can be found online at https://doi.org/10.1016/j.celrep.2024.114008.

ACKNOWLEDGMENTS

This work was supported by the Helmholtz Pioneer Campus, the eIslet project of the BMBF (grant number 031L0251), and ERC Consolidator Grant (number 772646). We thank Daniel Kokotek, Ioannis Deligiannis, Celia Martinez, Inti I.A. de la Rosa Velazquez and G. Eckstein for helping with the sample preparation and performing the NovaSeq sequencing. We thank Stefan Veit, Revanth Coimbatore Varadarajan, and Che-Wei Chang for manufacturing of the chips. Further we thank Thomas Schwarz-Romond for critically reading the manuscript.

AUTHOR CONTRIBUTIONS

C.R., M. Marder, M. Meier, and B.S. designed the study. C.R. and M. Marder executed biological experiments. M.O. and J.A.P. designed and characterized the chip, which is based on a previous design from M. Moussus. C.R. and M. Marder performed the scRNA-seq processing and did the analysis. C.R., M. Marder, J.B., and A.F. performed stainings on chip. C.R. and M. Marder did the image analysis. C.v.T. did the mass spectrometric measurements and data processing. M. Meier received the funding and supervised the study. The manuscript was written by C.R., M. Marder, and M. Meier. All authors corrected and approved the paper.

DECLARATION OF INTERESTS

J.A.P, M.O., and M. Meier filed a patent application for the OoC technology described herein.

Received: September 13, 2023
Revised: January 25, 2024
Accepted: March 12, 2024
Published: March 26, 2024

REFERENCES

1. Ricard, N., Bailly, S., Guignabert, C., and Simons, M. (2021). The quiescent endothelium: signalling pathways regulating organ-specific endothelial normalcy. Nat. Rev. Cardiol. *18*, 565–580. https://doi.org/10.1038/s41569-021-00517-4.
2. Trimm, E., and Red-Horse, K. (2023). Vascular endothelial cell development and diversity. Nat. Rev. Cardiol. *20*, 197–210. https://doi.org/10.1038/s41569-022-00770-1.
3. Xu, S., Ilyas, I., Little, P.J., Li, H., Kamato, D., Zheng, X., Luo, S., Li, Z., Liu, P., Han, J., et al. (2021). Endothelial Dysfunction in Atherosclerotic Cardiovascular Diseases and Beyond: From Mechanism to Pharmacotherapies. Pharmacol. Rev. *73*, 924–967. https://doi.org/10.1124/pharmrev.120.000096.
4. von Scheidt, M., Zhao, Y., Kurt, Z., Pan, C., Zeng, L., Yang, X., Schunkert, H., and Lusis, A.J. (2017). Applications and Limitations of Mouse Models for Understanding Human Atherosclerosis. Cell Metabol. *25*, 248–261. https://doi.org/10.1016/j.cmet.2016.11.001.

5. Tran, V., De Silva, T.M., Sobey, C.G., Lim, K., Drummond, G.R., Vinh, A., and Jelinic, M. (2020). The Vascular Consequences of Metabolic Syndrome: Rodent Models, Endothelial Dysfunction, and Current Therapies. Front. Pharmacol. *11*, 148.
6. Patsch, C., Challet-Meylan, L., Thoma, E.C., Urich, E., Heckel, T., O'Sullivan, J.F., Grainger, S.J., Kapp, F.G., Sun, L., Christensen, K., et al. (2015). Generation of vascular endothelial and smooth muscle cells from human pluripotent stem cells. Nat. Cell Biol. *17*, 994–1003. https://doi.org/10.1038/ncb3205.
7. Kennedy, C.C., Brown, E.E., Abutaleb, N.O., and Truskey, G.A. (2021). Development and Application of Endothelial Cells Derived From Pluripotent Stem Cells in Microphysiological Systems Models. Front. Cardiovasc. Med. *8*, 625016.
8. Rosowski, S., Remmert, C., Marder, M., Akishiba, M., Bushe, J., Feuchtinger, A., Platen, A., Ussar, S., Theis, F., Wiedenmann, S., and Meier, M. (2023). Single-cell characterization of neovascularization using hiPSC-derived endothelial cells in a 3D microenvironment. Stem Cell Rep. *18*, 1972–1986. https://doi.org/10.1016/j.stemcr.2023.08.008.
9. Williams, I.M., and Wu, J.C. (2019). Generation of Endothelial Cells From Human Pluripotent Stem Cells. Arterioscler. Thromb. Vasc. Biol. *39*, 1317–1329. https://doi.org/10.1161/ATVBAHA.119.312265.
10. Vila Cuenca, M., Cochrane, A., van den Hil, F.E., de Vries, A.A.F., Lesnik Oberstein, S.A.J., Mummery, C.L., and Orlova, V.V. (2021). Engineered 3D vessel-on-chip using hiPSC-derived endothelial- and vascular smooth muscle cells. Stem Cell Rep. *16*, 2159–2168. https://doi.org/10.1016/j.stemcr.2021.08.003.
11. Cochrane, A., Albers, H.J., Passier, R., Mummery, C.L., van den Berg, A., Orlova, V.V., and van der Meer, A.D. (2019). Advanced in vitro models of vascular biology: Human induced pluripotent stem cells and organ-on-chip technology. Adv. Drug Deliv. Rev. *140*, 68–77. https://doi.org/10.1016/j.addr.2018.06.007.
12. Campinho, P., Vilfan, A., and Vermot, J. (2020). Blood Flow Forces in Shaping the Vascular System: A Focus on Endothelial Cell Behavior. Front. Physiol. *11*, 552.
13. Helle, E., Ampuja, M., Antola, L., and Kivelä, R. (2020). Flow-Induced Transcriptomic Remodeling of Endothelial Cells Derived From Human Induced Pluripotent Stem Cells. Front. Physiol. *11*, 591450.
14. Nguyen, D.-H.T., Stapleton, S.C., Yang, M.T., Cha, S.S., Choi, C.K., Galie, P.A., and Chen, C.S. (2013). Biomimetic model to reconstitute angiogenic sprouting morphogenesis in vitro. Proc. Natl. Acad. Sci. USA *110*, 6712–6717. https://doi.org/10.1073/pnas.1221526110.
15. Hajal, C., Offeddu, G.S., Shin, Y., Zhang, S., Morozova, O., Hickman, D., Knutson, C.G., and Kamm, R.D. (2022). Engineered human blood–brain barrier microfluidic model for vascular permeability analyses. Nat. Protoc. *17*, 95–128. https://doi.org/10.1038/s41596-021-00635-w.
16. Trietsch, S.J., Israëls, G.D., Joore, J., Hankemeier, T., and Vulto, P. (2013). Microfluidic titer plate for stratified 3D cell culture. Lab Chip *13*, 3548–3554. https://doi.org/10.1039/C3LC50210D.
17. Zhang, X., Bishawi, M., Zhang, G., Prasad, V., Salmon, E., Breithaupt, J.J., Zhang, Q., and Truskey, G.A. (2020). Modeling early stage atherosclerosis in a primary human vascular microphysiological system. Nat. Commun. *11*, 5426. https://doi.org/10.1038/s41467-020-19197-8.
18. Madamanchi, N.R., Vendrov, A., and Runge, M.S. (2005). Oxidative stress and vascular disease. Arterioscler. Thromb. Vasc. Biol. *25*, 29–38. https://doi.org/10.1161/01.ATV.0000150649.39934.13.
19. Roux, E., Bougaran, P., Dufourcq, P., and Couffinhal, T. (2020). Fluid Shear Stress Sensing by the Endothelial Layer. Front. Physiol. *11*, 861.
20. Rhodes, J.M., and Simons, M. (2007). The extracellular matrix and blood vessel formation: not just a scaffold. J. Cell Mol. Med. *11*, 176–205. https://doi.org/10.1111/j.1582-4934.2007.00031.x.
21. Traag, V.A., Waltman, L., and van Eck, N.J. (2019). From Louvain to Leiden: guaranteeing well-connected communities. Sci. Rep. *9*, 5233. https://doi.org/10.1038/s41598-019-41695-z.
22. McInnes, L., Healy, J., and Melville, J. (2020). UMAP: Uniform Manifold Approximation and Projection for Dimension Reduction. Preprint at arXiv. https://doi.org/10.48550/arXiv.1802.03426.
23. Muhl, L., Genové, G., Leptidis, S., Liu, J., He, L., Mocci, G., Sun, Y., Gustafsson, S., Buyandelger, B., Chivukula, I.V., et al. (2020). Single-cell analysis uncovers fibroblast heterogeneity and criteria for fibroblast and mural cell identification and discrimination. Nat. Commun. *11*, 3953. https://doi.org/10.1038/s41467-020-17740-1.
24. McCracken, I.R., Dobie, R., Bennett, M., Passi, R., Beqqali, A., Henderson, N.C., Mountford, J.C., Riley, P.R., Ponting, C.P., Smart, N., et al. (2022). Mapping the developing human cardiac endothelium at single-cell resolution identifies MECOM as a regulator of arteriovenous gene expression. Cardiovasc. Res. *118*, 2960–2972. https://doi.org/10.1093/cvr/cvac023.
25. Dekker, R.J., van Thienen, J.V., Rohlena, J., de Jager, S.C., Elderkamp, Y.W., Seppen, J., de Vries, C.J.M., Biessen, E.A.L., van Berkel, T.J.C., Pannekoek, H., and Horrevoets, A.J.G. (2005). Endothelial KLF2 Links Local Arterial Shear Stress Levels to the Expression of Vascular Tone-Regulating Genes. Am. J. Pathol. *167*, 609–618. https://doi.org/10.1016/S0002-9440(10)63002-7.
26. Bae, Y.S., Oh, H., Rhee, S.G., and Yoo, Y.D. (2011). Regulation of Reactive Oxygen Species Generation in Cell Signaling. Mol. Cell. *32*, 491–509. https://doi.org/10.1007/s10059-011-0276-3.
27. Galbusera, M., Zoja, C., Donadelli, R., Paris, S., Morigi, M., Benigni, A., Figliuzzi, M., Remuzzi, G., and Remuzzi, A. (1997). Fluid shear stress modulates von Willebrand factor release from human vascular endothelium. Blood *90*, 1558–1564.
28. Fang, J.S., Coon, B.G., Gillis, N., Chen, Z., Qiu, J., Chittenden, T.W., Burt, J.M., Schwartz, M.A., and Hirschi, K.K. (2017). Shear-induced Notch-Cx37-p27 axis arrests endothelial cell cycle to enable arterial specification. Nat. Commun. *8*, 2149. https://doi.org/10.1038/s41467-017-01742-7.
29. Magid, R., Murphy, T.J., and Galis, Z.S. (2003). Expression of matrix metalloproteinase-9 in endothelial cells is differentially regulated by shear stress. Role of c-Myc. J. Biol. Chem. *278*, 32994–32999. https://doi.org/10.1074/jbc.M304799200.
30. Morancho, A., Ma, F., Barceló, V., Giralt, D., Montaner, J., and Rosell, A. (2015). Impaired Vascular Remodeling after Endothelial Progenitor Cell Transplantation in MMP9-Deficient Mice Suffering Cortical Cerebral Ischemia. J. Cerebr. Blood Flow Metabol. *35*, 1547–1551. https://doi.org/10.1038/jcbfm.2015.180.
31. Morawietz, H., Wagner, A.H., Hecker, M., and Goettsch, W. (2008). Endothelin receptor B-mediated induction of c-jun and AP-1 in response to shear stress in human endothelial cells. Can. J. Physiol. Pharmacol. *86*, 499–504. https://doi.org/10.1139/Y08-026.
32. Wettschureck, N., Strilic, B., and Offermanns, S. (2019). Passing the Vascular Barrier: Endothelial Signaling Processes Controlling Extravasation. Physiol. Rev. *99*, 1467–1525. https://doi.org/10.1152/physrev.00037.2018.
33. Bergen, V., Lange, M., Peidli, S., Wolf, F.A., and Theis, F.J. (2020). Generalizing RNA velocity to transient cell states through dynamical modeling. Nat. Biotechnol. *38*, 1408–1414. https://doi.org/10.1038/s41587-020-0591-3.
34. Hautefort, A., Pfenniger, A., and Kwak, B.R. (2019). Endothelial connexins in vascular function. Vasc. Biol. *1*, H117–H124. https://doi.org/10.1530/VB-19-0015.
35. Zeng, Y., He, J., Bai, Z., Li, Z., Gong, Y., Liu, C., Ni, Y., Du, J., Ma, C., Bian, L., et al. (2019). Tracing the first hematopoietic stem cell generation in human embryo by single-cell RNA sequencing. Cell Res. *29*, 881–894. https://doi.org/10.1038/s41422-019-0228-6.
36. Tabula Sapiens Consortium*; Jones, R.C., Karkanias, J., Krasnow, M.A., Pisco, A.O., Quake, S.R., Salzman, J., Yosef, N., Bulthaup, B., Brown, P., et al. (2022). The Tabula Sapiens: A multiple-organ, single-cell transcriptomic atlas of humans. Science *376*, eabl4896. https://doi.org/10.1126/science.abl4896.

37. Schilling, K., Opitz, N., Wiesenthal, A., Oess, S., Tikkanen, R., Müller-Esterl, W., and Icking, A. (2006). Translocation of Endothelial Nitric-Oxide Synthase Involves a Ternary Complex with Caveolin-1 and NOSTRIN. Mol. Biol. Cell *17*, 3870–3880. https://doi.org/10.1091/mbc.E05-08-0709.
38. Murthy, S., Koval, O.M., Ramiro Diaz, J.M., Kumar, S., Nuno, D., Scott, J.A., Allamargot, C., Zhu, L.J., Broadhurst, K., Santhana, V., et al. (2017). Endothelial CaMKII as a regulator of eNOS activity and NO-mediated vasoreactivity. PLoS One *12*, e0186311. https://doi.org/10.1371/journal.pone.0186311.
39. Abu Taha, A., Taha, M., Seebach, J., and Schnittler, H.-J. (2014). ARP2/3-mediated junction-associated lamellipodia control VE-cadherin–based cell junction dynamics and maintain monolayer integrity. Mol. Biol. Cell *25*, 245–256. https://doi.org/10.1091/mbc.E13-07-0404.
40. Poznyak, A.V., Nikiforov, N.G., Markin, A.M., Kashirskikh, D.A., Myasoedova, V.A., Gerasimova, E.V., and Orekhov, A.N. (2020). Overview of OxLDL and Its Impact on Cardiovascular Health: Focus on Atherosclerosis. Front. Pharmacol. *11*, 613780.
41. Ghosh, A., Gao, L., Thakur, A., Siu, P.M., and Lai, C.W.K. (2017). Role of free fatty acids in endothelial dysfunction. J. Biomed. Sci. *24*, 50. https://doi.org/10.1186/s12929-017-0357-5.
42. Wang, Y.L., Hui, Y.N., Guo, B., and Ma, J.X. (2007). Strengthening tight junctions of retinal microvascular endothelial cells by pericytes under normoxia and hypoxia involving angiopoietin-1 signal way. Eye *21*, 1501–1510. https://doi.org/10.1038/sj.eye.6702716.
43. Duvigneau, J.C., Esterbauer, H., and Kozlov, A.V. (2019). Role of Heme Oxygenase as a Modulator of Heme-Mediated Pathways. Antioxidants *8*, 475. https://doi.org/10.3390/antiox8100475.
44. Rogero, M.M., and Calder, P.C. (2018). Obesity, Inflammation, Toll-Like Receptor 4 and Fatty Acids. Nutrients *10*, 432. https://doi.org/10.3390/nu10040432.
45. Luo, W., Wang, Y., Yang, H., Dai, C., Hong, H., Li, J., Liu, Z., Guo, Z., Chen, X., He, P., et al. (2018). Heme oxygenase-1 ameliorates oxidative stress-induced endothelial senescence via regulating endothelial nitric oxide synthase activation and coupling. Aging *10*, 1722–1744. https://doi.org/10.18632/aging.101506.
46. Di Pietro, P., Oliveti, M., Sommella, E., Damato, A., Puca, A., Ciaglia, E., Levkau, B., Carnevale, R., Iacoviello, L., Di Castelnuovo, A., et al. (2020). Sortilin evokes endothelial dysfunction and arterial hypertension through the dysregulation of sphingolipid metabolism and oxidative stress. Eur. Heart J. *41*, ehaa946.2704. https://doi.org/10.1093/ehjci/ehaa946.2704.
47. Uhlén, M., Karlsson, M.J., Hober, A., Svensson, A.-S., Scheffel, J., Kotol, D., Zhong, W., Tebani, A., Strandberg, L., Edfors, F., et al. (2019). The human secretome. Sci. Signal. *12*, eaaz0274. https://doi.org/10.1126/scisignal.aaz0274.
48. Sangwung, P., Zhou, G., Nayak, L., Chan, E.R., Kumar, S., Kang, D.-W., Zhang, R., Liao, X., Lu, Y., Sugi, K., et al. (2017). KLF2 and KLF4 control endothelial identity and vascular integrity. JCI Insight *2*, e91700. https://doi.org/10.1172/jci.insight.91700.
49. Lundberg, J.O., and Weitzberg, E. (2022). Nitric oxide signaling in health and disease. Cell *185*, 2853–2878. https://doi.org/10.1016/j.cell.2022.06.010.
50. Jiang, H., Zhou, Y., Nabavi, S.M., Sahebkar, A., Little, P.J., Xu, S., Weng, J., and Ge, J. (2022). Mechanisms of Oxidized LDL-Mediated Endothelial Dysfunction and Its Consequences for the Development of Atherosclerosis. Front. Cardiovasc. Med. *9*, 925923. https://doi.org/10.3389/fcvm.2022.925923.
51. López-Novoa, J.M., and Bernabeu, C. (2010). The physiological role of endoglin in the cardiovascular system. Am. J. Physiol. Heart Circ. Physiol. *299*, H959–H974. https://doi.org/10.1152/ajpheart.01251.2009.
52. Lilly, B., Dammeyer, K., Marosis, S., McCallinhart, P.E., Trask, A.J., Lowe, M., and Sawant, D. (2018). Endothelial cell-induced cytoglobin expression in vascular smooth muscle cells contributes to modulation of nitric oxide. Vasc. Pharmacol. *110*, 7–15. https://doi.org/10.1016/j.vph.2018.06.016.
53. Liu, B., and Dai, Z. (2022). Fatty Acid Metabolism in Endothelial Cell. Genes *13*, 2301. https://doi.org/10.3390/genes13122301.
54. Ekmekçi, O.B., and Ekmekçi, H. (2006). Vitronectin in atherosclerotic disease. Clin. Chim. Acta *368*, 77–83. https://doi.org/10.1016/j.cca.2005.12.015.
55. Yaghoubi, A., Ghojazadeh, M., Abolhasani, S., Alikhah, H., and Khaki-Khatibi, F. (2015). Correlation of Serum Levels of Vitronectin, Malondialdehyde and Hs- CRP With Disease Severity in Coronary Artery Disease. J. Cardiovasc. Thorac. Res. *7*, 113–117. https://doi.org/10.15171/jcvtr.2015.24.
56. Papaioannou, T.G., and Stefanadis, C. (2005). Vascular wall shear stress: basic principles and methods. Hellenic J. Cardiol. *46*, 9–15.
57. Wang, Y.I., and Shuler, M.L. (2018). UniChip enables long-term recirculating unidirectional perfusion with gravity-driven flow for microphysiological systems. Lab Chip *18*, 2563–2574. https://doi.org/10.1039/C8LC00394G.
58. Olmer, R., Engels, L., Usman, A., Menke, S., Malik, M.N.H., Pessler, F., Göhring, G., Bornhorst, D., Bolten, S., Abdelilah-Seyfried, S., et al. (2018). Differentiation of Human Pluripotent Stem Cells into Functional Endothelial Cells in Scalable Suspension Culture. Stem Cell Rep. *10*, 1657–1672. https://doi.org/10.1016/j.stemcr.2018.03.017.
59. Wolock, S.L., Lopez, R., and Klein, A.M. (2019). Scrublet: Computational Identification of Cell Doublets in Single-Cell Transcriptomic Data. Cell Syst. *8*, 281–291.e9. https://doi.org/10.1016/j.cels.2018.11.005.
60. Compera, N., Atwell, S., Wirth, J., Wolfrum, B., and Meier, M. (2021). Upscaling of pneumatic membrane valves for the integration of 3D cell cultures on chip. Lab Chip *21*, 2986–2996. https://doi.org/10.1039/D1LC00194A.
61. Schindelin, J., Arganda-Carreras, I., Frise, E., Kaynig, V., Longair, M., Pietzsch, T., Preibisch, S., Rueden, C., Saalfeld, S., Schmid, B., et al. (2012). Fiji: an open-source platform for biological-image analysis. Nat. Methods *9*, 676–682. https://doi.org/10.1038/nmeth.2019.
62. Tinevez, J.-Y., Perry, N., Schindelin, J., Hoopes, G.M., Reynolds, G.D., Laplantine, E., Bednarek, S.Y., Shorte, S.L., and Eliceiri, K.W. (2017). TrackMate: An open and extensible platform for single-particle tracking. Methods *115*, 80–90. https://doi.org/10.1016/j.ymeth.2016.09.016.
63. Schmidt, U., Weigert, M., Broaddus, C., and Myers, G. (2018). Cell Detection with Star-convex Polygons, pp. 265–273. https://doi.org/10.1007/978-3-030-00934-2_30.
64. Wolf, F.A., Angerer, P., and Theis, F.J. (2018). SCANPY: large-scale single-cell gene expression data analysis. Genome Biol. *19*, 15. https://doi.org/10.1186/s13059-017-1382-0.
65. La Manno, G., Soldatov, R., Zeisel, A., Braun, E., Hochgerner, H., Petukhov, V., Lidschreiber, K., Kastriti, M.E., Lönnerberg, P., Furlan, A., et al. (2018). RNA velocity of single cells. Nature *560*, 494–498. https://doi.org/10.1038/s41586-018-0414-6.
66. Bondareva, O., Rodríguez-Aguilera, J.R., Oliveira, F., Liao, L., Rose, A., Gupta, A., Singh, K., Geier, F., Schuster, J., Boeckel, J.-N., et al. (2022). Single-cell profiling of vascular endothelial cells reveals progressive organ-specific vulnerabilities during obesity. Nat. Metab. *4*, 1591–1610. https://doi.org/10.1038/s42255-022-00674-x.
67. Abdelmagid, S.A., Clarke, S.E., Nielsen, D.E., Badawi, A., El-Sohemy, A., Mutch, D.M., and Ma, D.W.L. (2015). Comprehensive profiling of plasma fatty acid concentrations in young healthy Canadian adults. PLoS One *10*, e0116195. https://doi.org/10.1371/journal.pone.0116195.
68. Compera, N., Atwell, S., Wirth, J., von Törne, C., Hauck, S.M., and Meier, M. (2022). Adipose microtissue-on-chip: a 3D cell culture platform for differentiation, stimulation, and proteomic analysis of human adipocytes. Lab Chip *22*, 3172–3186. https://doi.org/10.1039/D2LC00245K.
69. Hladik, D., Dalke, C., von Toerne, C., Hauck, S.M., Azimzadeh, O., Philipp, J., Ung, M.-C., Schlattl, H., Rößler, U., Graw, J., et al. (2020). CREB Signaling Mediates Dose-Dependent Radiation Response in the Murine Hippocampus Two Years after Total Body Exposure. J. Proteome Res. *19*, 337–345. https://doi.org/10.1021/acs.jproteome.9b00552.

70. Navarro, P., Trevisan-Herraz, M., Bonzon-Kulichenko, E., Núñez, E., Martínez-Acedo, P., Pérez-Hernández, D., Jorge, I., Mesa, R., Calvo, E., Carrascal, M., et al. (2014). General Statistical Framework for Quantitative Proteomics by Stable Isotope Labeling. J. Proteome Res. *13*, 1234–1247. https://doi.org/10.1021/pr4006958.

71. Benjamini, Y., and Hochberg, Y. (1995). Controlling the False Discovery Rate: A Practical and Powerful Approach to Multiple Testing. J. Roy. Stat. Soc. B *57*, 289–300. https://doi.org/10.1111/j.2517-6161.1995.tb02031.x.

72. Raudvere, U., Kolberg, L., Kuzmin, I., Arak, T., Adler, P., Peterson, H., and Vilo, J. (2019). g:Profiler: a web server for functional enrichment analysis and conversions of gene lists (2019 update). Nucleic Acids Res. *47*, W191–W198. https://doi.org/10.1093/nar/gkz369.

73. Kuleshov, M.V., Jones, M.R., Rouillard, A.D., Fernandez, N.F., Duan, Q., Wang, Z., Koplev, S., Jenkins, S.L., Jagodnik, K.M., Lachmann, A., et al. (2016). Enrichr: a comprehensive gene set enrichment analysis web server 2016 update. Nucleic Acids Res. *44*, W90–W97. https://doi.org/10.1093/nar/gkw377.

STAR★METHODS

KEY RESOURCES TABLE

REAGENT or RESOURCE	SOURCE	IDENTIFIER
Antibodies		
VE-Cadherin, rabbit	Cell Signaling	RRID: AB_2077970
PECAM-1, rabbit	Thermo Fisher Scientific	RRID: AB_10981955
DLL4, rabbit	Cell Signaling	RRID: AB_2800263
ARP3, mouse	Sigma Aldrich	RRID: AB_476749
KLF4, rabbit	Thermo Fisher Scientific	RRID: AB_2898967
Claudin5,	Thermo Fisher Scientific	RRID: AB_2809891
Angiopoietin2	Thermo Fisher Scientific	RRID: AB_2544773
PECAM-1, mouse	Cell Signaling	RRID: AB_2160882
Alexa Fluor 555, donkey anti-rabbit	Thermo Fisher Scientific	RRID: AB_162543
Alexa Fluor 488, donkey anti-mouse	Thermo Fisher Scientific	RRID: AB_141607
Alexa Fluor 647, goat anti-mouse	Thermo Fisher Scientific	RRID: AB_2535809
CD31-FITC	BD	Cat#555445; RRID AB_395838
CD140b-PE	BD	Cat#558821; RRID:AB_397132
Chemicals, recombinant proteins		
FITC-dextran 2000 kDa	Sigma Aldrich	FD2000S
DAPI	Sigma Aldrich	D9542
Live/Dead Viability/Toxicity Kit	Thermo Fisher Scientific	L3224
Collagenase P	Roche	11213857001
oxLDL	Thermo Fisher Scientific	L34357
Dil-oxLDL	Thermo Fisher Scientific	L34358
BODIPY	Thermo Fisher Scientific	D3922
Phalloidin-Atto-647	Abcam	ab176759
Hoechst33342	Thermo Fisher Scientific	62249
TBHP	abcam	ab113851
TY52156	Sigma Aldrich	5330620001
Pro3dure GR-10 resin	Litholabs	HX10031
VEGFA	Peprotech	100-20-250
FGF2	Miltenyi Biotec	130-093-838
CHIR99021	Axon Medchem BV	1385
BMP4	PeproTech	120-05ET-10
Forskolin	Abcam	Ab120058
Critical commercial assays		
Fluorometric Nitric Oxide Assay Kit	Sigma Aldrich	482655-1KIT
Chromium Next GEM Single Cell 3′ Kit v3.1	10x Genomics	1000269
Chromium Next GEM Chip G Single Cell Kit	10x Genomics	1000127
NovaSeq SP flow cell	Illumina	
PreOmics' iST Kit	Preomics GmbH	P.O.00001
Green fluorescent CellROX	Sigma Aldrich	C10444
Experimental models: Cell lines		
HiPSC	HMGUi001-A	
Software and algorithms		
Python (version 3.9.12)	python	https://www.python.org/
Jupyter lab (version 3.4.8)	jupyter	https://jupyter.org/

(*Continued on next page*)

Continued

REAGENT or RESOURCE	SOURCE	IDENTIFIER
Scrublet	Wolock et al.[59]	https://github.com/swolock/scrublet
Scanpy (version 1.9.1)	Scverse project	https://github.com/scverse/scanpy
scVelo (version 0.2.5)	Theis lab	https://github.com/theislab/scvelo
All source code files used within this paper are published on Github	Meier lab	GitHub: https://github.com/MeierLabMiBioEng/StemCell-derivedVessel-on-chip
Deposited data		
All scRNA seq data sets are deposited at GEO.		Accession code GSE253320
Other		
Fibronectin	Thermo Fisher Scientific	33010018
StemPro-34	Thermo Fisher Scientific	10639011
FBS	Sigma	F7524
Double-sided adhesive foil	ARcare	90445Q
Polypropylene filament	SERAG-WIESSNER GmbH	CP05341A
Polystyrene particles	microParticles GmbH	PS-F-B237-1
Accutase	Sigma Aldrich	A6964
EGM-2	Sigma Aldrich	C-22011
B27 supplement	Life Technologies	21103049/12587010
hESC-Matrigel	Corning	354277
mTeSR1 medium	StemCell Technologies	85850

RESOURCE AVAILABILITY

Lead contact

Further information and requests for resources and reagents should be directed to and will be fulfilled by the lead contact, Matthias Meier (matthias.meier@uni-leipzig.de).

Materials availability

This study did not generate reagents.

Data and code availability

- Single-cell RNA-seq data have been deposited at GEO and are publicly available as of the date of publication. Accession numbers are listed in the key resources table.
- The code for scRNA-seq analysis has been deposited on GitHub and is publicly available. The GitHub webpage link is listed in the key resources table.
- Any additional information required to reanalyze the data reported in this paper is available from the corresponding author upon request.

EXPERIMENTAL MODEL AND STUDY PARTICIPANT DETAILS

Experiments were conducted using a hiPSC line, which was kindly provided by Prof. Lickert (Helmholtz Zentrum Munich) and is registered in the human pluripotent stem cell registry (https://hpscreg.eu) under the name HMGUi002-A. The cell line was derived from a Caucasian male donor.

METHOD DETAILS

Generation and cultivation of SC-ECs

Human iPSCs were cultured on hESC Matrigel-precoated 6-plates according to manufacturer's recommendations (Corning, Cat#354277) in mTeSR1 medium (StemCell Technologies, Cat#85850) at 5% CO2, 5% O2 and 37°C with daily medium change and passaged twice a week in a 1:6 ratio using 0.05% Trypsin-EDTA (Sigma Aldrich, Cat#T4174). The hiPSC culture was free of mycoplasma contamination as tested by the MycoSensor PCR assay kit (Agilent Technology, Cat#302109).

For the differentiation, the hiPSCs were transferred into a 3D cell culture format. Therefore, the medium was aspirated, cells were washed with 2 mL PBS −/−, and 500 μL Accutase (Sigma Aldrich, Cat#A6964) was added. During incubation at 37°C for 5 min, cells detached. Addition of 2.5 mL mTeSR stopped the Accutase reaction. The well was washed with 1 mL mTeSR before centrifugation for 5 min at 200 x g and resuspended in 500 μL mTeSR with Rock inhibitor Y-27632 dihydrochloride 10μM (Abcam, Cat# HY-10583) and 1% Penicillin/Streptomycin (P/S) (Thermo Fisher Scientific, Cat#15140122). Cells were transferred in 6-well ultra-low attachment plates (Corning, Cat#3471) at a cell concentration of $5*10^5$ cells/ml and in 3 mL volume. The plate was placed on an orbital shaker in the cell incubator and rotated at a frequency of 100rpm.

The differentiation protocol was adopted from Rosowski et al.[6,58] From day zero to day three of differentiation Neurobasal Medium with B27 supplement (Life Technologies, Cat# 21103049 and 12587010) supplemented with BMP4 (25 ng/mL) (PeproTech, Cat#120-05ET-10) and CHIR 99021 (7.5 μM) (Axon Medchem BV, Cat# 1385) was used without media change. Media was changed daily from day three to seven of differentiation using StemPro-34 (Life Technologies, Cat#10639011) with VEGFA (200 ng/mL) (PeproTech, Cat#10-20-100) and forskolin (2 μM) (Abcam, Cat#ab120058). Afterward, StemPro-34 with VEGFA (30 ng/mL) and FGF2 (30 ng/mL) (Miltenyi Biotech, Cat#130-093-838) was used with exchange after two days until use.

Successful differentiation was determined by flow cytometry analysis and staining for the EC marker CD31-FITC (BD, Cat#555445) and the smooth muscle cell marker CD140b-PE (BD, Cat#558821). For purification, SC-ECs were FACS sorted (MACSTyto Cell Sorter, Miltenyi Biotec, according to manufactures protocol) leading to an SC-EC population of >90%. Standard SC-EC culture was performed on fibronectin coated plates (Sigma, 5 μg/mL final concentration) in StemPro-34 medium supplemented with 15% FBS (Sigma, Cat#F7524), 100 ng/mL VEGFA and 100 ng/mL FGF2. Medium change was done every other day.

Cryopreservation and passaging of SC-ECs

SC-ECs could be passaged and were used until passage 6. For passaging, cells were washed with PBS−/− and detached with Accutase. The reaction was stopped with StemPro-34 medium followed by a centrifugation at 200*g* and 5 min. SC-ECs were resuspended in supplemented StemPro-34 medium and seeded in a 1:2 ratio in T75 flasks. For cryopreservation, detached SC-ECs were resuspended in FBS with 10% DMSO.

Chip manufacturing

For the OoC production, chips were printed using an Asiga Pico 2 HD UV 3D printer and Pro3dure GR-10 resin (clear, transparent, Litholabs, HX10031). Slice thickness was set to 50 μm. As described before, the anti-aliasing method[60] was used to compensate for errors in the 3D printed part by smoothening the chips channels to a round shape. After printing, channels were flushed with Isopropanol and chips were washed and ultrasonicated for 15 min in Isopropanol. After removing all uncured resin, chips were dried at 80°C for 30 min and UV-flashed in an N_2 atmosphere with 2000 flashes on each side using an Otoflash G171. For biocompatibility treatment, chips were incubated in 99% EtOH for 24 h and transferred to MilliQ water for 24 h. For the chip assembly, polyamide monofilaments (1005215; efco creative GmbH, Germany) were cut with a sharp scalpel and fed through the medium reservoirs and the gel chamber. The chip was bonded to a glass slide with a double-sided adhesive foil (ARcare 90445Q). To seal the chip, polydimethylsiloxan (PDMS) was into the outer chambers and cured for 15 min at 80°C. For sterilization, the chips were placed for 30 min under UV light prior to hydrogel filling.

Flow characterization

Microchannels were created in the OoC with a polypropylene filament of diameter 50 μm (CP05341A; SERAG-WIESSNER GmbH) and polyamide filament of diameter 150 μm and 250 μm (1005215, 1005225; efco creative GmbH). 80 μL PBS were placed on top of the gels. 100 μL PBS with 0.1% 2.55 μm polystyrene particles (PS-F-B237-1; microParticles GmbH) were added to both sides of the chip. Chips were placed on a Zeiss AxioObserver at angles of 7°, 13°, and 25° to induce gravity-driven flow. Particle flow rates were recorded with a frame rate of 700 fps and exposure time of 1/20000 s for 5 s at 5, 30, 60, 120, 180 and 240 s after tilting. Buffer was allowed to level out on both sides before subsequent recordings. For cyclic measurements, chips were rotated every 2 min and particles were recorded 5, 30, 60 and 120 s after the start of every cycle. Recorded videos were analyzed in Fiji (ImageJ[61]) using the TrackMate[62] plugin (v6.0.1) and flow rate measurements were exported to R (v4.2.0) for further analysis. Wall shear stress values (τ_w) were calculated using a derivation of the Hagen-Poiseuille equation, where μ is the dynamic viscosity of serum-free media (0.73 mPa s; Poon et al., 2020), *U* is the mean flow velocity and *R* is the radius of the lumen.

$$\tau_w = \frac{4\mu U}{R}$$

Cell seeding on chip

For cell seeding on chip, a collagen type I hydrogel (Corning ref. 354236) was neutralized for pH = 7.0 with the appropriate proportions of 10xPBS,1 mM NaOH and H20 to obtain 2.5 mg mL^{-1}, mixed thoroughly and placed for 1 h on ice. Meanwhile, sterile chips were cooled down to −20°C. The collagen gel was filled into the gel chamber (40 μL/chamber) and polymerized for 40 min at 37°C. SC-ECs were detached with Accutase and concentrated to 4x 10^6 cells per mL for seeding. Cells were resuspended thoroughly and 30 μL were added to the inlet and outlet chambers. The filament was pulled out of the outlet chamber using forceps to introduce gravitation-driven flow of cell suspension into the generated lumen. Chips were placed on a rocking shaker (OrganoFlow L, Mimetas) at a 10° angle and 6 rpm for 15 min. After initial seeding, EGM-2 (Sigma Aldrich, C-22011) medium was added to all chambers (30 µL/chamber). Chips for the flow condition were placed back on the shaker at a 25° angle and 2 min intervals. Complete medium change was performed after 2 h and then every day (70 µL/chamber). The open microfluidic system allows for high throughput handling as the medium change takes less than 1 min per chip using a multistep pipette and using a cell culture pump for aspiration through a filter-less 10 µL tip.

Whole mount immunofluorescence staining

For whole mount staining on chip, cells were fixed with 4% PFA for 15 min at RT and washed with PBS afterward. Samples were permeabilized with PBS +0.1% Triton X-100 for 30 min at RT, washed with PBS-T and blocked for 2 h with blocking buffer (PBS-T, 10% FBS, 1% BSA, 0.1M glycine, 3% donkey serum). Chips were stained in blocking buffer without glycine for 2 days at 4°C. Primary antibodies were washed out thoroughly with PBS-T for 1 h before secondary antibodies were added in blocking buffer without glycine. Secondary antibodies were incubated overnight at 4°C. Next, samples were washed with PBS-T and mounted in Vectashield for imaging.

Histology of lumen sections

Cell-laden lumens could be retrieved from the chip body by breaking the connecting structures of the insert with a scalpel. The hydrogel block was transferred to a well plate with tweezers, washed with PBS and fixed with 4% PFA. Paraffin embedding was initiated the same day according to standard procedures. 3 µm thick sections were stained with primary antibodies. Nuclei were identified with Hoechst 33342. Fluorescence stainings were digitalized with an AxioImager 7 (Zeiss, Oberkochen, Germany) equipped with a 20× objective, and visualized with the Zeiss Zen Blue Software.

Confocal imaging

Wholemount stained lumens were imaged on a confocal microscope (Zeiss Axio Observer LSM 880, Zeiss Zen black software). Images of VE-Cadherin, DAPI staining and brightfield PMT of the whole lumen including outgrowing branches were taken (20× magnification, 0.26 µm per pixel, 10 µm z-stacks). For visualization of COL1 fibers, blank lumens were prepared, fixed and imaged profiting from label-free imaging via confocal reflection microscopy.

Lumen permeability analysis

To test the lumens for endothelial barrier function, the lumens were perfused with 50 µL FITC-Dextran (diluted 1:10 in PBS, 2000 and 40 kDa, Sigma Aldrich, FD2000S) in the inlet chamber. Images were taken every 3 min for 20 min with an epi-fluorescent microscope (Zeiss Axio Observer Z1) using an automated imaging template for the chip designed with the Zeiss Zen Blue software. For analysis, 3 lines transverse to the lumen were set through each captured image in distance of 50 µm (Figure 2E). Those lines were measured for signal intensity from left to right. Next, the signal intensities from left to right were plotted in a Jupyter notebook script. To consider for the lumen not being exactly centered in the middle of the image, the maximum of each curve was set as x = 0. Then, all FITC-dextran intensities of all lumens from one condition could be mean-plotted into one curve.

Branching characterization and branch density analysis

For branch analysis, Z-stacks from VE-Cadherin-stained confocal images defined as ''only covering lumen bottom'' were converged to a 3D-projection in Fiji. 3D-stacked images were batch-filtered in Fiji (i.e., CLAHE, Otsudark auto-threshold, median filter, binarized). For branching characterization, Fiji's ''skeletonize 2D/3D'' and ''Analyze skeleton 2D/3D″ tools were applied on filtered and binarized images (Figure S2B). For density analysis, filtered and binarized images were measured for signal density (as a percentage of black over white signal) using a MATLAB script. Signal intensities of longitudinal lines were measured which were directing with 1 µm from each other from the central lumen towards the periphery branches. For each parallel line a mean signal intensity was measured, and those mean intensities could then be plotted in dependence from their distance from the central lumen resulting in the signal density plot. The output data of skeleton and density analysis were further processed in Python.

Live dead cell analysis

ECs cultivated under flow were stained on day 2 with Live/Dead Viability/Toxicity Kit (LIFE Technologies - L3224) as described in the manufacturer's protocol. Stained lumens were imaged on an epifluorescence microscope (Zeiss, Zen software). For image analysis, signal intensities were normalized to an auto-threshold and a StarDist segmentation FIJI plug-in[63] was applied to detect live and dead cells. The mean signal threshold for both markers were set to 3000 and the mean area threshold to 50 μm^2.

NO assay

For measuring the NO production in ECs, the fluorometric Nitric Oxide Assay Kit (Sigma) was used according to the manufacture protocol. The assay is based on the enzymatic conversion of nitrate to nitrite so that the total amount of nitric oxide in the supernatant can be analyzed. For each condition a respective background control was carried along and background fluorescence was substracted after measurement. For normalization, cells were extracted from the lumen and counted.

Sample preparation for scRNA-seq

For RNA single cell sequencing, chips were washed with PBS. To ensure that only cells growing in the hydrogel were collected, inlet and outlet ports were blocked with 3% agarose. After solidification of the agarose, cells were treated with a 1:1 mix of Collagenase P (18 U final concentration, Roche 11213857001) and Accutase and incubated for 30 min at 37°C. Pipette tips and tubes were washed with PBS +2% BSA before usage to reduce cell loss. Successfully dissolved hydrogels and a single cell suspension was confirmed under the microscope before harvesting the cells in PBS +10% FBS. The cells were centrifuged at 300 x g for 3 min, washed with PBS +2% BSA and filtered with a 20 μm cell Pluristrainer (pluriSelect, 43-50020-023). Cells were counted with TrypanBlue (Sigma) and a cell vitality of over 70% was confirmed. RNA libraries were generated using Chromium Single Cell 3′ library and gel bead kit v3.1 (10x Genomics). The amplified cDNA library was sequenced on a NovaSeq SP flow cell from Illumina.

Pre-processing of scRNA-seq data

Raw sequencing data files were demultiplexed, aligned (reference genome hg38_ensrel96), filtered, barcodes and UMIs counted, and subjected to a quality filter with CellRanger (10xGenomics). The pre-processing and downstream analysis were performed with the package ‘Scanpy[64] API’88 in python with default parameters, if not stated differently. Cell-ranger processed data from static and flow condition were first concatenated. Next, dead or stressed cells, identified by a percentage of mitochondrial genes higher than 15%, were filtered out. Cells with less than 3000 or more than $6x10^4$ total counts or cells with less than 200 expressed genes were excluded. Also, genes expressed in less than 10 cells were rejected. Afterward, gene counts were normalized to 10^4 per cell and log transformed. Additionally, cell cycle genes and mitochondrial genes were regressed out. Doublets were detected with the Scrublet package.[59]

Clustering and cell type annotation

The single-cell neighborhoods were calculated with the first 30 principal components and 10 nearest neighbors and the cells were clustered with the Leiden algorithm[21] at a resolution of 0.5. For visualization, UMAP was used to reduce the dimensionality of the data. Cell types were annotated by ranking the top 25 marker genes of each of the 7 Leiden sub-cluster based on literature research. Correlation plots confirmed similarity of subclusters. Cell type proportions and gene expression analysis were performed based on the defined categorical clusters.

RNA velocity using basic modeling

To investigate developmental trajectories in the flow sample, we analyzed the RNA velocity by recovering directed dynamic gene information through splicing kinetics in basic mode following the scVelo[33] standard pipeline. Variables and observations, like cluster annotation and UMAP coordinates were accessed from the Scanpy analysis as described above. The splicing matrix was generated by default settings of the velocyto[65] pipeline. After concatenating splice matrix and scanpy information, splice variants and cells were filtered, normalized, and logarithmized with the function scv.pp.filter_and_normalize (shared_counts = 20, n_top_genes = 2000). In the next step, the moments, based on the connectivity, were calculated with 30 PCAs and 30 neighbors. Then, velocities and the based root cell were assessed by the sc.velo algorithm and represented in an UMAP embedding stream projection.

Cell treatment for oxidative stress induction

ECs were seeded and cultured under flow for 1 day as described above. For oxidative stress induction, either 50 μg mL^{-1} oxLDL (life technologies) or 800 μM FFA-BSA mixture was added to EGM2 medium from day 1 to day 2. An FFA stock was prepared in advance consisting of a mixture of different fatty acids dissolved in ethanol: c14:0 (1.05%), c16:0 (26.75%), c18:0 (8.04%), c18:2 (36.63%), c18:1 (21.09%) and c20:4 (6.44%; all from Sigma) as described in Bondareva et al..[66] These candidates are a selection of the most common free fatty acids in human serum and the chosen percentual combination was measured in human serum.[67] For FFA-BSA treatment solution, an 8 mM stock solution was generated by conjugating the fatty acids to fatty acid-free BSA (Sigma). Therefore, a mixture of BSA, FFA and high-grade Ethanol (9: 0.8: 0.2) was incubated for 2h at 37°C and 1500 rpm. When described, sortilin inhibitor TY52156 was added in a concentration of 100 nM from day 1 on together with oxidative stress induction. On day 2, the EGM2 was replaced by serum free medium (DMEM/F12 + Glutamax +1% P/S) and the treatment was continued until day 3. On day 3, supernatants were collected for secretome analysis and immediately frozen and stored at −80°C. Afterward the chips were washed four times for 1h with PBS before hydrogels were digested in a 1:1 mix of Collagenase P and Accutase. Cells were collected, washed three times with PBS and pelleted. Lysates were stored at −80°C until mass spectrometry preparation. Medium and untreated cell samples were carried along as controls. As the FFA treated sample contained BSA, the control was treated with a BSA-Ethanol-vehicle control.

Sample preparation and mass spectrometry measurements

Lysate pellets were prepared for mass spectrometry measurement as described in Compera et al.[68] Supernatants were digested enzymatically using the PreOmics’ iST Kit (Preomics GmbH, Martinsried, Germany) including the SP3 add-on kit according to manufacturers’ specifications with adjustment of volumes for the SP3-lyse and -binding buffers to fulfill 1x concentration of buffers. After drying, the peptides were resuspended in 2% acetonitrile (ACN) and 0.5% trifluoroacetic acid. The HRM Calibration Kit (Biognosys, Schlieren, Switzerland) was added to all samples according to the manufacturer's instructions. MS data were acquired on a Q Exactive (QE) high field (HF) mass spectrometer (Thermo Fisher Scientific Inc.) as described in Hladik et al.[69]

Data processing - protein identification

Proteome Discoverer 2.5 software (Thermo Fisher Scientific; version 2.5.0.400) was used for peptide and protein identification via a database search (Sequest HT search engine) against Swissprot human database (Release 2020_02, 20432 sequences), considering full tryptic specificity, allowing for one missed tryptic cleavage sites, precursor mass tolerance 10 ppm, fragment mass tolerance 0.02 Da. Carbamidomethylation of Cys was set as a static modification. Dynamic modifications included deamidation of Asn, Gln, oxidation of Met; and a combination of Met loss with acetylation on protein N terminus. Percolator was used for validating peptide spectrum matches and peptides, accepting only the top-scoring hit for each spectrum, and satisfying the cutoff values for FDR $<1\%$, and posterior error probability <0.05. The Sequest HT Xcorr filter was set to 1.6 removing identifications below this threshold. The final list of proteins complied with the strict parsimony principle.

Data processing - Label-free quantification

Proteins were quantified based on abundance values for unique peptides. Abundance values were first normalized to the total amount of peptides in each sample to account for sample loading errors. The protein abundances were calculated summing up the abundance values for admissible peptides. The final protein ratio between experimental groups was calculated using median values of single peptide ratios per comparison. The statistical significance of the ratio change was ascertained employing the t test method described in Navarro et al.[70] Adjusted p values are calculated according to Benjamini-Hochberg.[71]

Data analysis

In the following downstream analysis, only proteins with more than one unique peptide hit were used. Differential protein expression (DEP) analysis was performed with customized Python (version 3.10) scripts using the adjusted p values (p.adj <0.05) and normalized abundance ratios (ratio >1.5). Differently expressed proteins were only taken into account, when abundances were measured in at least 75% of the replicates within each group. In addition, the secretome data was filtered for actively secreted proteins matching the DEP against the refined human secretome.[47] Only proteins with the labels "blood secretion" were used. Enrichment analysis and Go term identification was performed using the STRING gprofiler[72] and Enrichr[73] databases and customized Python scripts from GitHub repository XDbit (https://github.com/jwrth/xDBiT_toolbox).

Oxidative stress compound staining

For staining of FFA accumulation, lumens were fixed on day 3 as described above, washed with PBS and incubated with BODIPY (4,4-difluoro-1,3,5,7,8- pentamethyl-4-bora-3a, 4a-diaza-*s*-indacene, Thermo, D3922) in a final concentration of 10 μg mL^{-1} in PBS, together with DAPI (Thermo, D9542, 1:100) and Phalloidin-Atto-647(ab176759, 1:200). For staining of oxLDL accumulation, lumens were treated as described for the oxLDL treatment with Dil-labelled oxLDL (Thermo, L34358) for 3 days. After fixation, lumens were stained with DAPI and Phalloidin-Atto-647 as described above. For detection of oxidative stress in cells, lumens were stained with greenfluorescent CellROX (Sigma, C10444). Lumens were washed 3 times in PBS, before CellROX was added in a final concentration of 5 μM in PBS together with Hoechst33342 (Thermo, 10 μg mL^{-1}) and incubated for 1h at 37°C in an incubator. After staining has been completed, lumens were fixed as described above and imaged with a confocal microscope under the same settings for all conditions. For a positive control, lumens were treated with 100 μM TBHP (abcam, ab113851). For image analysis of CellROX signal, for each capture a z stack consisting of 6 slices with distance of 6 μm was converted to one stack image by 3D projection in fiji. Then, Stardist segmentation program was applied comparable to the live-dead staining. The mean signal intensity was set to 5 and the mean area threshold were set to 5 μm^2 for both the DAPI and CellROX channel. For later analysis in a Python script, fragmented, apoptotic and highly bright nuclei were further filtered, setting an area threshold of 60 μm^2. Due to technical-related differences in DAPI and CellROX staining intensities, for each image the CellROX signal intensity was normalized to its corresponding DAPI signal intensity, resulting in a normalized CellROX/DAPI intensity ratio for each image.

QUANTIFICATION AND STATISTICAL ANALYSIS

Statistical analysis was performed using the scipy.stats function with custom-written python code. Statistical details of experiments and numbers of replicates can be found in the figure legends. Data was tested for normal distribution with the Shapiro test and for homogeneous variances with the Levene or Bartlett test. Statistical significance between groups was tested with a pairwise t test for two conditions and with a one-way ANOVA for multiple sample groups followed by a Tukeys post-hoc test.